MODELING OF MECHANICAL BEHAVIOUR OF ANISOTROPIC ROCKS

By Aida Rezapour, M.ENG.

A Thesis Submitted to the School of Graduate Studies in Partial Fulfillment of the Requirements for the Degree Master of Applied Science.

McMaster University

MASTER OF APPLIED SCIENCE (2015)   McMaster University

(Civil Engineering)   Hamilton, Ontario

TITLE: MODELING   OF   MECHANICAL   BEHAVIOUR   OF

                                        ANISOTROPIC ROCKS

AUTHOR: Aida Rezapour, M.ENG.

SUPERVISOR: Dr. S.Pietruszczak,

NUMBER OF PAGES: viii, 74

Abstract

The natural soils and sedimentary rocks are typically formed by deposition and progressive consolidation of marine sediments. Consequently, they are characterized by the presence of closely spaced bedding planes, resulting in anisotropy in their mechanical behaviour. Among anisotropic rocks, the group of sedimentary rocks known as shales is of a particular interest as it is often the host rock in nuclear waste storage and oil industry. The Tournemire shales are anisotropic in terms of deformability and the failure mode, which means that complex constitutive models should be used to describe their mechanical response.

In this thesis a pragmatic methodology based on the notion of a microstructure tensor, as suggested by Pietruszczak and Mroz (2001), has been employed for the description of orientation dependent characteristics of Tournemire shale. This has been combined with a plasticity framework that incorporates an anisotropic deviatoric hardening. The formulation requires identification of several parameters including strength descriptors associated with the failure criterion and constants that are involved in describing the anisotropy and strain hardening. All the material functions/parameters have been identified here based on the experimental results reported by Niandou et al. (1997). Using those parameters, the numerical simulations of a number of triaxial tests were conducted and the results compared with the experimental data in order to verify the performance of the model.

After the verification stage, the formulation was incorporated in a commercial FE code (Abaqus/standard) using the **UMAT** interface and was then applied to a numerical analysis of a tunnel excavation within the anisotropic rock mass. The numerical results, including the distribution of the damage and vertical/horizontal displacements, have been compared for different orientations of the bedding planes.

Acknowledgement

I would like to express my special appreciation and gratitude to my advisor Professor S. Pietruszczak. His useful advice, comments, remarks and engagement throughout the process of completion of this master thesis was priceless. His support encouraged me to continuously strive for excellence in my graduate student career.

I am also grateful to Professor S. Chidiac and Professor T. Becker for their time spent on examining this thesis.

A special thanks to my family for all their love and encouragement. Words cannot express how grateful I am to my parents for all of the sacrifices and supports they have made on my behalf. And most of all, I would like to express deep appreciation and thanks to my beloved husband Ehsan who always supported me.

Table of Contents

List of Figures

List of Tables

1.   Introduction

The natural soils and sedimentary rocks such as shale, slate, gneiss, and schist are typically formed by deposition and progressive consolidation during the diagenesis. Such formations usually have a distinct internal structure, which is characterized by the appearance of multiple sedimentary layers or bedding planes. Consequently, the mechanical characteristics display an inherent anisotropy. Inherent anisotropy is strongly linked with the microstructural arrangement, e.g. crack pattern, bedding planes, foliation, presence of joints and micro/ macro fissures, etc. Anisotropy may also occur in granular media, but it is mostly associated with sedimentary rocks. Deformation behavior and failure mode of these materials are strongly dependent on the loading orientation with respect to the microstructure arrangement. Typically, the inherent anisotropy in a soil or rock takes the form of transverse-isotropy characterized by one direction with distinctive anisotropy perpendicular to an isotropic bedding or lamination plane (Kirkgard & Lade, 1993; Abelev & Lade, 2004; Niandou et al., 1997). This direction, normally coincident with the direction of deposition, is referred to as the axis of anisotropy and the plane is referred to as the plane of transverse-isotropy.

Over the last few decades, an extensive research effort has been dedicated to study the mechanical behaviour of anisotropic rocks. Comprehensive references on this topic can be found in a number of papers (Amadei, 1983; Kwasniewski, 1993; Ramamurthy, 1993). The notion of transverse isotropy in geomaterials has been studied primarily through triaxial tests, and has been found of a significant importance in the analysis and design of a variety of geotechnical structures, such as foundations, retaining walls and slopes (Casagrande & Carillo, 1944; Arthur & Menzies, 1972; Oda et al.,1978).

Experimental evidence indicates that most sedimentary rocks display an anisotropy of strength and deformation (Donath, 1964; Colak & Unlu, 2004; Hoek, 1964; McLamore & Gray, 1967; Horino & Ellickson, 1970a; Kwasniewski, 1993; Ramamurthy, 1993; Nasseri et al., 2003; Colak & Unlu, 2004; Karakul et al., 2010) and the degree of anisotropy varies

from one sedimentary rock to another. Some geological formations behave more anisotropically than others due to well defined bedding planes (Chappell, 1990).

The strength anisotropy of diverse types of rocks have been investigated by many researchers. As an example, Donath, (1964), McLamore & Gray, (1967) and Attewell & Sandford, (1974) conducted a series of triaxial experimentation on slate. Chenevert & Gatlin, (2013) evaluated the directional properties of two type of shales using a triaxial compression cell and auxiliary stress - strain measuring equipment. Colak & Unlu, (2004) investigated the strength of anisotropic intact rocks using the data from compressive (uniaxial and triaxial) and indirect tensile (Brazilian) tests. Brown et al., (1977) studied the Shear strength characteristics of Delabole slate. Deklotz et al., (1966) conducted several direct tension and unconfined and triaxial compression tests in order to investigate the anisotropic behaviour of a schistose gneiss. Martin McCabe and Koerner, (1975) studied the changes in friction and cohesion of Mica schist tested in tension and compression at different orientations. They also examined the fracture surfaces by use of a scanning electron microscope. Nasseri et al., (2003) evaluated the failure pattern of four anisotropic schistose rocks in macro and micro scale with the aid of unconfined and confined triaxial compression tests. Behrestaghi et al., (1996), conducted uniaxial and triaxial tests on schists by considering different orientation of schistosity with respect to the major principal stress. Ramamurthy et al., (1988) and Rao et al., (1986) focussed on two intrinsically anisotropic phyllites which were tested in high pressure triaxial apparatus. They proposed a simple strength criterion based on experimental results of these anisotropic rocks. Sandstones were investigated by Horino and Ellickson, (1970), Arora, (1987) and Al-Harthi, (1998) by conducting uniaxial compressive strength tests. Pomeroy et al., (1971) evaluated the anisotropy of coal by use of a triaxial compression apparatus and applying a uniaxial compressive load. Tien & Tsao, (2000) studied the strength anisotropy of artificial rock-like materials which represent the anisotropic behavior of rocks such as shale, slate and sandstone. Uniaxial and triaxial compression tests were performed on these artificial interlayered rocks. Angabini, (2003) investigated on limestone. The stress–strain behaviors were determined by uniaxial strength, tensile strength and shear strength tests. Ajalloeian

and Lashkaripour, (2000) concentrated on performing uniaxial compression tests on two anisotropic mudrocks (siltshale and mudshale). Salager et al., (2012) assessed the transverse isotropic behaviour of Opalinus clay using several triaxial tests and Niandou et al., (1997) conducted triaxial compression tests for studying the strength anisotropy of Tournemire shale.

A large number of triaxial compression tests have been conducted on oriented samples (H. Niandou et al., 1997, Donath, 1961; McLamore & Gray, 1967; Attewell & Sandford, 1974; Hoek, 1983). By reviewing the experimental evidence, investigators generally concluded that maximum failure strength is either at $\beta = 0°$ or $\beta = 90°$ and the minimum value usually is within the range $30 - 60°$, where β is the angle between major principal stress and the plane of weakness, fracture or sliding. The studies on the effects of bedding plane orientation on the elastic properties of anisotropic rocks reveal that the Young's modulus normal to bedding plane is lower than along bedding plane (Chenevert & Gatlin, 2013).

Experimental data by Halidou et al. (1994), have shown that in most rock materials, plastic deformation is generally coupled with damage due to development of microcracks. The damage is typically associated with strain softening. In the paper by Chen et al. (2010), a constitutive model for plastic and damage modeling of anisotropic materials has been suggested. Their work is an extension of the plastic model proposed by Pietruszczak et al. (2002) by considering induced damage caused by micro cracks.

The directional dependence of strength is an important property that should be taken into account in the analysis of different geostructures. For the safety analysis of structures constructed in such geological formations, it is important to develop constitutive models able to account for influence of structural anisotropy. Therefore, in addition to experimental research, an extensive research has been carried out on formulation of appropriate general failure criteria and plastic deformation. A comprehensive review on this topic, examining different approaches, is provided in the article by Duveau et al. (1998).

In general, the formulation of anisotropic models follows different approaches. The primary methodologies are derived either from the extension of isotropic criteria and introduce several parameters that change with loading orientation or are proposed by considering the concept of discontinuous weakness planes (Walsh and Brace, 1964; McLamore and Gray, 1967; Hoek and Brown, 1980; Ramamurthy, 1993; Jaeger, 2009). These criteria require a large amount of experimental data and curve fitting. Also it's difficult to relate certain parameters to the microstructure of the rock. In view of this, they are not very convenient for use in complex engineering applications.

The second approach is based on incorporating fabric tensors of different orders in the failure function (Boehler, 1978; Cazacu and Cristescu, 1998). Such an approach is very complex and also the parameter identification from experimental data is difficult. Therefore, this methodology does not seem appropriate for use in practical problems.

The third family of models involves incorporation of the second order microstructure tensor (Ken-Ichi, 1984; Qiang et al., 2001; Chen et al., 2010; Chen et al., 2012). Here, the most pragmatic formulation is perhaps the one that employs a scalar anisotropy parameter which is expressed in terms of mixed invariants of the stress and structure-orientation tensors. This approach was effectively applied to failure criterion of anisotropic rocks (Pietruszczak and Mroz, 2001). The same methodology was also used for deriving an elastoplastic model for anisotropic sedimentary rocks (Pietruszczak et al., 2002). The model can be used in practical engineering problems and in comparison with the other approaches, does not require a large number of laboratory tests to estimate its parameters. Also, the mathematical formulation is not overly complex.

In this thesis one type of sedimentary rock is considered, namely Tournemile shale, which consists of both clay and silt and has a laminated or fissile texture. Since shales have low porosity and permeability, time dependent effects associated with pressure diffusion and ionic convection should be considered. Capillary effects between diphasic fluids could also play an important role (Schmitt et al., 1994). Shales are widely used in nuclear waste storage and in oil industry. In the latter case, the extra drilling cost attributed to shale-

instability problems is often very substantial prompting extensive research into this topic (Schmitt et al., 1994). It should be mentioned that the mechanical behavior of shales, due to their high clay content, is very sensitive to the saturation state. An extensive investigation on the effects of degree of saturation on the physical/mechanical properties for Tournemire shale has been presented in the article by Vales et al., (2004).

This research thesis contains six chapters. The next chapter discusses the formulation of two simplified failure criteria for anisotropic materials with emphasising on microstructure tensor approach. A complete plasticity framework incorporating this failure function in specification of deformation characteristics in anisotropic sedimentary rocks is then discussed. The third chapter provides the numerical scheme that is used for integrating the elastoplastic constitutive equations. In the fourth chapter the identification of basic material parameters, which are required in applying microstructure tensor formulation, is discussed and several numerical simulations that verify the performance of the model are presented. The results are compared with the experimental data; in particular the results of tests reported by Niandou et al., (1997) are considered. Chapter five deals with application of this methodology in Finite Element analysis. This chapter provides a numerical example solved by Abaqus which deals with the assessment of damage in a tunnel excavated in Tournemire shale. The geometry, boundary and initial conditions related to this model is taken from a paper by Le & Nguyen, (2014). The last chapter provides conclusions and recommendation for future work.

2.   Formulation of anisotropic failure criteria

2.1   Introduction

The formulation of failure criteria for anisotropic materials constitutes an important problem which has attracted the attention of numerous researchers. An extensive review and assessment of various failure functions can be found in a paper by Duveau et al. (1998). The analytical formulations usually employ linear and second order terms in stress components referred to principal material axes. An example here is the orthotropic criterion formulated by Hill (1948) for metals, which was subsequently extended by Tsai and Wu (1971) for composite materials and by Pariseau (1968) for rocks. A more general approach which employs ten independent basic and mixed invariants of stress and microstructure tensors was introduced by Boehler and Sawczuk(1970). Cowin (1986), also used a similar formulation and developed a simplified approximation in which the failure criterion is defined as a quadratic function of stress and fabric tensors. Another approach to formulate the failure criteria involves the notion of the existence of a critical plane, or the weakest orientation, along which the failure function reaches a maximum (Hoek and Brown, 1980; Hoek, 1983; Walsh and Brace, 1964). More recently, the problem was also formulated by invoking the notion of a fabric tensor specifying the directional distribution of lineal/areal porosity (Pietruszczak, 1999). The main difficulty with implementation of these approaches is the fact that they require a large number of material parameters and/or functions to be identified.

In this chapter, two simplified approaches are discussed. The first one is the critical plane approach, which employs a spatial distribution of strength parameters (Pietruszczak and Mroz, 2001). This criterion requires a development of a constrained optimization procedure in order to define the orientation of the critical plane. The second approach, which is the main focus of this thesis, is based on the structure-orientation tensors (Pietruszczak and Mroz , 2001). This framework employs a scalar anisotropy parameter η defined in terms of mixed invariants of stress and microstructure tensors. A complete plasticity formulation

incorporating the microstructure tensor for determining the deformation characteristics is discussed in Pietruszczak (2010).

2.2   Specification of conditions at failure based on critical plane approach

The approach employs a spatial distribution of strength parameters and the orientation of the critical plane can be defined by maximizing the failure function with respect to the orientation. The failure function, F, is defined in terms of tangential and normal traction components, τ and σ, acting on a plane with unit normal n_i.

$$F = f(\tau, \sigma) - c(n_i) \tag{2.1}$$

where

$$\tau = \sigma_{ij} n_i s_j; \quad \sigma = \sigma_{ij} n_i n_j; \quad n_i s_i = 0 \tag{2.2}$$

And s_i is an arbitrary unit vector normal to n_i . In equation (2.1), $c(n_i)$ is a scalar valued function defined over a unit sphere and it may be assumed in the form

$$c(n_i) = c_0 \left(1 + \Omega_{ij} n_i n_j + \Omega_{ijkl} n_i n_j n_k n_l + \Omega_{ijklmn} n_i n_j n_k n_l n_m n_n + \cdots \right) \tag{2.3}$$

where Ω's are symmetric traceless tensors of even rank describing the bias in the spatial distribution and c_0 is a constant. For simplicity, the higher order tensors may be defined as dyadic products

$$\Omega_{ijkl} = b_1 \Omega_{ij} \Omega_{kl}; \qquad \Omega_{ijklmn} = b_2 \Omega_{ij} \Omega_{kl} \Omega_{mn} \quad .... \tag{2.4}$$

which yields

$$c(n_i) = c_0 \left(1 + \Omega_{ij} n_i n_j + b_1 (\Omega_{ij} n_i n_j)^2 + b_2 (\Omega_{ij} n_i n_j)^3 + \cdots \right) \tag{2.5}$$

 In representation (2.5), it is assumed that eigenvectors of Ω_{ij} coincide with the principal material axes. For transversely isotropic material there is only one independent eigenvalue of Ω_{ij} (since $\Omega_{ii} = 0$), while for an isotropic material Ω_{ij} vanishes.

If $b_1 = b_2 = ... = 0$, then,

$$c(n_i) = c_0 \left(1 + \Omega_{ij} n_i n_j\right) \tag{2.6}$$

In this case, the constant c_0 is the orientation average of $c(n_i)$.

The onset of failure and specification of the orientation of the critical plane can be formulated as a constrained optimization problem, i.e.

$$\max_{n_i, s_i} F = \max_{n_i, s_i} \left(f(\sigma, \tau) - c(n_i)\right) = 0; \quad n_i n_i = 1, \ n_i s_i = 0, \ s_i s_i = 1 \tag{2.7}$$

Alternatively, one can define the tangential traction as

$$\tau = \left\|t_k^s\right\| = \left\|\left(\delta_{ki} - n_k n_i\right)\sigma_{ij} n_j\right\| \tag{2.8}$$

so that

$$\max_{n_i} F = \max_{n_i} \left(f(\sigma, \tau) - c(n_i)\right) = 0; \quad n_i n_i = 1 \tag{2.9}$$

The above equations can be solved by Lagrange multipliers or any other suitable optimization technique. The solution provides the orientation of the critical/localization plane and defines the conditions at which the failure occurs.

2.2.1   *Example: Mohr-coulomb criterion*

Assuming that both strength parameters, c and μ, are orientation dependent and have linear form analogous to that employed in equation (2.6), this criterion can be written as

$$\max_{n_i, s_i} F = \max_{n_i, s_i} \left(\tau + \mu\sigma - c \right) = 0 \qquad (2.10)$$

Where

$$\mu = \mu_0(1 + \Omega_{kl}^{\mu} n_k n_l), \;\; c = c_0(1 + \Omega_{ij}^{c} n_i n_j) \qquad (2.11)$$

Here, μ represents the tangent of internal friction angle and c is referred to as cohesion. The failure function, F, may now be defined as

$$F = \left| \sigma_{ij} n_i s_j \right| + \mu_0(1 + \Omega_{kl}^{\mu} n_k n_l)\sigma_{ij} n_i n_j - c_0(1 + \Omega_{ij}^{c} n_i n_j) \qquad (2.12)$$

For the constraints given in equation (2.7), the Lagrangian function may be constructed as

$$\begin{aligned} G = &\left| \sigma_{ij} n_i s_j \right| + \mu_0(1 + \Omega_{kl}^{\mu} n_k n_l)\sigma_{ij} n_i n_j - c_0(1 + \Omega_{ij}^{c} n_i n_j) \\ &- \lambda_1(n_i n_i - 1) - \lambda_2 n_i s_i - \lambda_3(s_i s_i - 1) \end{aligned} \qquad (2.13)$$

Where λ_1, λ_2 and λ_3 are the Lagrangian multipliers. The stationary conditions with respect to n_i and s_i take the form

$$\begin{aligned} \frac{\partial G}{\partial n_i} = &(S\sigma_{ij} - \lambda_2\delta_{ij})s_j - 2(-\mu_0\sigma_{ij} + c_0\Omega_{ij}^{c} + \lambda_1\delta_{ij})n_j \\ &+ 2\mu_0(\Omega_{ip}^{\mu}\sigma_{jk} + \Omega_{jp}^{\mu}\sigma_{ik})n_p n_j n_k = 0 \\ \frac{\partial G}{\partial s_i} = &(S\sigma_{ij} - \lambda_2\delta_{ij})n_j - 2\lambda_3 s_i = 0 \end{aligned} \qquad (2.14)$$

where $S = \mathrm{sgn}(\sigma_{ij} n_i s_j)$. By solving equations (2.14) simultaneously along with constraints in (2.7), the orientation of critical plane, n_i and s_i, as well as the Lagrangian multipliers may be determined.

2.3   Formulation of anisotropic failure criteria in terms of microstructure tensor

The present formulation incorporates scalar anisotropy parameters that are functions of invariants of stress and microstructure tensors. A microstructure tensor represents a measure of material fabric such as arrangement of intergranular contacts, pore size distribution, distribution of cracks in the damaged material, etc. It is defined as

$$a_{ij} = a_1 e_i^{(1)} e_j^{(1)} + a_2 e_i^{(2)} e_j^{(2)} + a_3 e_i^{(3)} e_j^{(3)} = a_1 m_{ij}^{(1)} + a_2 m_{ij}^{(2)} + a_3 m_{ij}^{(3)} \tag{2.15}$$

where a_1, a_2, a_3 are the principal values of the microstructure tensor and $m_{ij}^{\alpha} = e_i^{\alpha} e_j^{\alpha}$ are the respective structure-orientation tensors.

The most general approach assumes that the failure criterion depends on both the stress and microstructure tensors, i.e.

$$\begin{aligned} F = F(\sigma_{ij}, a_{ij}) &= F(T_{ip}T_{jq}\sigma_{pq}, T_{ip}T_{jq}a_{pq}) \\ &= F[\mathrm{tr}\sigma, \mathrm{tr}\sigma^2, tr\sigma^3, tra, tra^2, tra^3, tr(\sigma a), tr(\sigma^2 a), tr(\sigma a^2), tr(\sigma^2 a^2)] = 0 \end{aligned} \tag{2.16}$$

where T_{ij} is the transformation tensor. The above formulation provides a general framework which is complex for practical engineering applications. A simpler approach can be defined by considering the failure condition to depend on the relative orientation of the principal axes of both, σ_{ij} and a_{ij} tensors. Considering the principal triad of the microstructure tensor and specifying the traction moduli (components of L_i) on the planes normal to principal axes, Figure 2.1, one can write
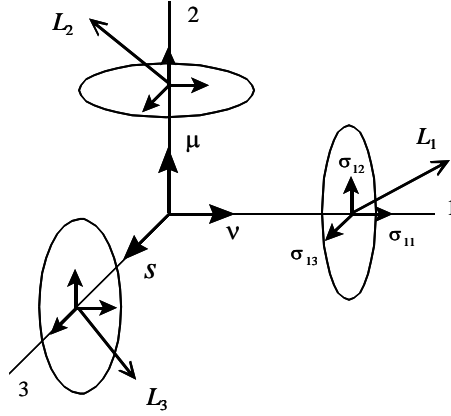
Figure 2. 1 Principal triad of the microstructure tensor a and the traction moduli L_1, L_2, L_3 (Pietruszczak and Mroz, 2001)

$$L_1 = (\sigma_{11}^2 + \sigma_{12}^2 + \sigma_{13}^2)^{1/2}; \quad L_2 = (\sigma_{12}^2 + \sigma_{22}^2 + \sigma_{23}^2)^{1/2}; \quad L_3 = (\sigma_{13}^2 + \sigma_{23}^2 + \sigma_{33}^2)^{1/2} \qquad (2.17)$$

A generalized loading vector, which is a unit vector along L_i, is defined as

$$l_i^2 = \frac{L_i^2}{L_k L_k} = \frac{e_k^{(i)} \sigma_{kj} e_m^{(i)} \sigma_{mj}}{\sigma_{pq} \sigma_{pq}} \qquad (2.18)$$

Note that

$$L_k L_k = L_1^2 + L_2^2 + L_3^2 = \sigma_{kj} \sigma_{kj} = tr(\sigma_{kl} \sigma_{lj}) = tr(\sigma^2) \qquad (2.19)$$

$$L_i^2 = e_k^{(i)} \sigma_{kj} e_l^{(i)} \sigma_{lj} = tr(m_{kp}^{(i)} \sigma_{ql} \sigma_{lk}) = tr(m^{(i)} \sigma^2) \qquad (2.20)$$

The projection of the microstructure tensor on the loading direction becomes

$$\eta = a_{ij} l_i l_j = a_1 \frac{tr(m^{(1)} \sigma^2)}{tr\sigma^2} + a_2 \frac{tr(m^{(2)} \sigma^2)}{tr\sigma^2} + a_3 \frac{tr(m^{(3)} \sigma^2)}{tr\sigma^2} = \frac{tr(a\sigma^2)}{tr(\sigma^2)} \qquad (2.21)$$

The scalar variable, η, is defined as the ratio of joint invariant of stress and microstructure tensor to the stress invariant and it identifies the effect of loading orientation relative to material axes. It is a homogeneous function of degree zero, so that stress magnitude does not affect its value (Pietruszczak and Mroz, 2000). This parameter is named as anisotropy

parameter since it reveals the orientation-dependent nature of the material strength. The equation (2.21) can be expressed as

$$\eta = \eta_0 \left(1 + A_{ij} l_i l_j \right) \tag{2.22}$$

where

$$A_{ij} = \mathrm{dev}(a_{ij})/\eta_0 \; ; \quad \eta_0 = \frac{1}{3} a_{kk} \tag{2.23}$$

Here, A_{ij} is a symmetric traceless operator and it is defined as the deviatoric part of the microstructure tensor normalized with respect to η_0. The former representation (2.22) can be generalized by considering higher order tensors

$$\eta = \eta_0 \left(1 + A_{ij} l_i l_j + A_{ijkl} l_i l_j l_k l_l + A_{ijklmn} l_i l_j l_k l_l l_m l_n + \cdots \right) \tag{2.24}$$

For simplicity, the higher order tensors can be replaced by dyadic products as follows

$$A_{ijkl} = b_1 A_{ij} A_{kl} \; ; \quad A_{ijklmn} = b_2 A_{ij} A_{kl} A_{mn} \tag{2.25}$$

so that

$$\eta = \eta_0 \left(1 + A_{ij} l_i l_j + b_1 (A_{ij} l_i l_j)^2 + b_2 (A_{ij} l_i l_j)^3 + \cdots \right) \tag{2.26}$$

where b's are constants.

Thus, the failure function (2.16) can now be expressed in a simplified form

$$F = F(\sigma, a) = F(tr\sigma, tr\sigma^2, tr\sigma^3, \eta) = 0 \tag{2.27}$$

As mentioned before, the value of parameter η is assumed to depend on the orientation of bedding planes relative to loading orientation. Thus, the existing failure criteria can be extended to anisotropic material by assuming that strength parameters change according to

equation (2.26). Generally, based on different types of materials and failure criteria which are used, several anisotropy parameters may be employed.

2.3.1 Plasticity formulation incorporating a microstructure tensor

In the previous section, failure condition for inherently anisotropic materials was presented. In this part, the approach is extended to the description of the inelastic deformation process, and the corresponding plasticity framework is discussed.

Considering the elastoplasticity framework, the general form of the yield/loading surface, as well as the plastic potential function, are as follows

$$f = f\left(\sigma, a, \varepsilon^p\right) = f\left(tr\sigma, tr\sigma^2, tr\sigma^3, \eta, \kappa\right) = 0 \tag{2.28}$$

$$\psi = \psi\left(\sigma, a\right) = \psi(tr\sigma, tr\sigma^2, tr\sigma^3, \eta) = const. \tag{2.29}$$

where κ is the scalar-valued function of irreversible deformation history. It should be mentioned that loading surface is defined in such a way that when $\kappa \to \infty$ »» $f \to F$, where F is the failure function.

The non-associated flow rule, which is essential in considering a progressive transition from compaction to dilatancy, can be expressed as

$$d\varepsilon_{ij}^p = d\lambda \frac{\partial \psi}{\partial \sigma_{ij}} \tag{2.30}$$

Imposing the consistency condition $df = 0$, yields

$$d\lambda = H_p^{-1} \frac{\partial f}{\partial \sigma_{ij}} d\sigma_{ij} \;\;;\;\; H_p = \frac{\partial f}{\partial \varepsilon_q^p} \left(dev \frac{\partial \psi}{\partial \sigma_{ij}} dev \frac{\partial \psi}{\partial \sigma_{ij}} \right)^{1/2} \tag{2.31}$$

where H_p is the plastic hardening modulus. More details on the formulation discussed here are provided in the next section, where a specific form of failure criterion is considered.

2.3.2   Illustrative example: Mohr-Coulomb criterion

The Mohr-Coulomb failure function for isotropic material can be written as

$$F = \sqrt{3}\bar{\sigma} - \eta_f g(\theta)\left(\sigma_m + C\right) = 0 \tag{2.32}$$

where

$$g(\theta) = \frac{3 - \sin\phi}{2\sqrt{3}\cos\theta - 2\sin\theta\sin\phi} \; ; \qquad \eta_f = \frac{6\sin\phi}{3 - \sin\phi} \; ; \qquad C = c\cot\phi \tag{2.33}$$

In the above equations, θ is equivalent to Lode's angle, ϕ and c are the angle of friction and cohesion, respectively. The stress measures $\bar{\sigma}$ and σ_m are defined as

$$\theta = \frac{1}{3}\sin^{-1}\left(\frac{-3\sqrt{3}}{2}\frac{J_3}{\bar{\sigma}^3}\right) \; \wedge \; -\frac{\pi}{6} \le \theta \le \frac{\pi}{6} \tag{2.34}$$

$$\bar{\sigma} = (J_2)^{1/2} \; ; \quad \sigma_m = -\frac{1}{3}I_1 \tag{2.35}$$

where I_1 and J_2 are the first stress invariant and second invariant of the stress deviator, respectively.

The above failure criterion can be straightforwardly extended to anisotropic regime by assuming that strength parameters, η_f and C, are orientation dependent. Thus, they both might have the representation consistent with equation (2.26), i.e.

$$\begin{aligned}
C &= C_0 \left(1 + C_{ij}l_il_j + a_1(C_{ij}l_il_j)^2 + a_2(C_{ij}l_il_j)^3 + \cdots\right) \\
\eta_f &= \eta_{f_0}\left(1 + A_{ij}l_il_j + b_1(A_{ij}l_il_j)^2 + b_2(A_{ij}l_il_j)^3 + \cdots\right)
\end{aligned} \tag{2.36}$$

In the framework of Mohr-Coulomb failure criterion, C is the strength under hydrostatic tension and is in fact independent of the orientation of the sample. For hydrostatic tension,

$$\sigma_{ij} = \delta_{ij} p_0 \tag{2.37}$$

and the loading vector components in equation (2.18) become invariant with respect to the orientation, that is

$$l_1 = l_2 = l_3 = 1/\sqrt{3} = const. \tag{2.38}$$

Thus, referring the problem to principal material axes x_i, in Figure 2. 2,

$$C_{ij} = 0 \text{ for } i \neq j \ ; \quad C_{ii} = 0 \quad \Rightarrow \quad C_{ij} l_i l_j = (C_1 + C_2 + C_3)/3 \equiv 0 \tag{2.39}$$

which indicates that $C = const.$ Therefore, in this case the only orientation dependent strength parameter is η_f .

$$\eta_f = \eta_{f_0} \left(1 + A_{ij} l_i l_j + b_1 (A_{ij} l_i l_j)^2 + b_2 (A_{ij} l_i l_j)^3 + \cdots \right) \ ; \quad C = const. \tag{2.40}$$

By examining the conditions at failure in samples having different orientation β with respect to loading direction, coefficients appearing in equation (2.40) can be identified, which will be described in details in chapter four.
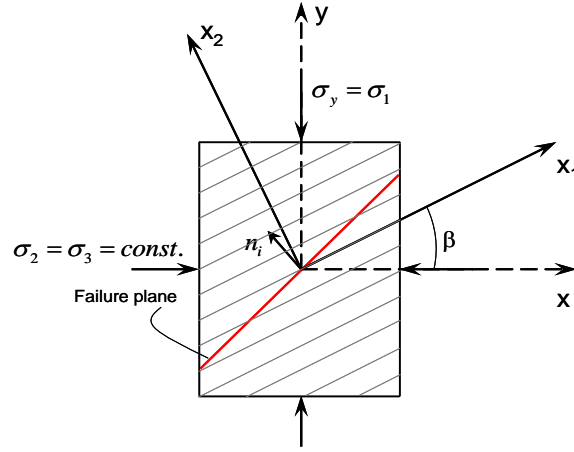
Figure 2. 2 principal material triad (Pietruszczak, 2010)

Consider now axial compression at confinement, P_0, and refer the problem to material axes as shown in Figure 2.2. In this case, the stress tensor in the local coordinate system of the sample $\{x_1, x_2\}$ may be defined as

$$\sigma_{ij} = T_{im}\sigma^*_{mn}T_{jn} = \begin{bmatrix} \cos^2(\beta)P_0 + \sin^2(\beta)\sigma_1 & -\cos(\beta)\sin(\beta)P_0 + \cos(\beta)\sin(\beta)\sigma_1 & 0 \\ -\cos(\beta)\sin(\beta)P_0 + \cos(\beta)\sin(\beta)\sigma_1 & \sin^2(\beta)P_0 + \cos^2(\beta)\sigma_1 & 0 \\ 0 & 0 & P_0 \end{bmatrix}$$

(2.41)

in which

$$T_{im} = \begin{bmatrix} \cos(\beta) & \sin(\beta) & 0 \\ -\sin(\beta) & \cos(\beta) & 0 \\ 0 & 0 & 1 \end{bmatrix} ; \quad \sigma^*_{mn} = \begin{bmatrix} p_0 & 0 & 0 \\ 0 & \sigma_1 & 0 \\ 0 & 0 & p_0 \end{bmatrix}$$

(2.42)

T_{im} is the transformation matrix and σ^*_{mn} is the stress tensor associated with triaxial tests. Using the representation above, the loading vector in equations (2.17) becomes

$$L_1^2 = \sigma_{11}^2 + \sigma_{12}^2 + \sigma_{13}^2 = \cos^2(\beta)P_0^2 + \sin^2(\beta)\sigma_1^2$$
$$L_2^2 = \sigma_{21}^2 + \sigma_{22}^2 + \sigma_{23}^2 = \sin^2(\beta)P_0^2 + \cos^2(\beta)\sigma_1^2 \tag{2.43}$$
$$L_3^2 = \sigma_{31}^2 + \sigma_{32}^2 + \sigma_{33}^2 = P_0^2$$

Now, the unit vector, l_i, along loading vector, L_i, can be expressed in the form

$$l_1^2 = \frac{L_1^2}{L_1^2 + L_2^2 + L_3^2} = \frac{\cos^2(\beta)P_0^2 + \sin^2(\beta)\sigma_1^2}{2P_0^2 + \sigma_1^2}$$
$$l_2^2 = \frac{L_1^2}{L_1^2 + L_2^2 + L_3^2} = \frac{\sin^2(\beta)P_0^2 + \cos^2(\beta)\sigma_1^2}{2P_0^2 + \sigma_1^2} \tag{2.44}$$
$$l_3^2 = \frac{L_1^2}{L_1^2 + L_2^2 + L_3^2} = \frac{P_0^2}{2P_0^2 + \sigma_1^2}$$

Considering transverse isotropy, the fabric tensor, A_{ij}, in the principal material axes

($A_{ij} = 0$ for $i \neq j$; $A_{ii} = 0$), may be identified as

$$A_{ij} = \begin{bmatrix} A_1 & 0 & 0 \\ 0 & A_2 & 0 \\ 0 & 0 & A_3 \end{bmatrix} \tag{2.45}$$

in which, $A_1 = A_3 = -0.5A_2$. Also note that $l_1^2 + l_2^2 + l_3^2 = 1$. Thus,

$$A_{ij}l_il_j = A_1l_1^2 + A_2l_2^2 + A_3l_3^2 = A_1l_1^2 - 2A_1l_2^2 + A_1l_3^2$$
$$= A_1(l_1^2 - 2l_2^2 + l_3^2) = A_1(1 - 3l_2^2) \tag{2.46}$$

Now, the equation (2.40) may be reduced to

$$\eta_f = \eta_{f_0}\left(1 + A_1(1 - 3l_2^2) + b_1A_1^2(1 - 3l_2^2)^2 + b_2A_1^3(1 - 3l_2^2)^3 + ...\right) \tag{2.47}$$

In the absence of confinement, when $P_0 = 0$, the anisotropy parameter is solely a function of deposition angle β

$$l_2 = \cos\beta \;\; \Rightarrow \;\; \eta_f = \eta_{f_0}\left(1 + A_1(1 - 3\cos^2\beta) + b_1 A_1^2(1 - 3\cos^2\beta)^2 + ...\right) \tag{2.48}$$

For defining the plasticity framework, the loading surface may be expressed as

$$f = \sqrt{3}\bar{\sigma} - \vartheta g(\theta)(\sigma_m + C) = 0 \tag{2.49}$$

in which

$$\vartheta = \vartheta(\kappa) = \eta_f \frac{\kappa}{A + \kappa} \;\; ; \;\; d\kappa = d\varepsilon_q^p = \frac{2}{\sqrt{3}}\sqrt{J_{2\dot{\varepsilon}^p}} \tag{2.50}$$

Here, $J_{2\dot{\varepsilon}}$ represents the second invariant of deviatoric plastic strain increment and B is a material constant. As mentioned before, when $\kappa \to \infty$ there is $\vartheta \to \eta_f$ that results in $f \to F$, which implies that the conditions at failure are compatible with Mohr-Coulomb criterion. The plastic potential may be defined as

$$\psi = \sqrt{3}\bar{\sigma} + \eta_c \, g(\theta)(\sigma_m + C)\ln\frac{(\sigma_m + C)}{\sigma_m^0} = 0 \tag{2.51}$$

where,

$$\eta_c = \alpha\eta_f \to \eta_c = \eta_c(l_i) \tag{2.52}$$

and σ_m^0 is evaluated from the condition of $\psi = 0$. Now pursuing the standard plasticity methodology and applying the consistency condition $df = 0$, yields

$$d\varepsilon_{ij}^p = d\lambda \frac{\partial \psi}{\partial \sigma_{ij}} ; \quad d\lambda = H_p^{-1} \frac{\partial f}{\partial \sigma_{ij}} d\sigma_{ij} ;$$

$$H_p = -\frac{2}{\sqrt{3}} \frac{\partial f}{\partial \vartheta} \frac{\partial \vartheta}{\partial \varepsilon_q^p} \left(dev \frac{\partial \psi}{\partial \sigma_{ij}} dev \frac{\partial \psi}{\partial \sigma_{ij}} \right)^{1/2}$$

(2.53)

For the considered Mohr-Coulomb functional form in equation (2.49), the gradient operator may be defined as

$$\frac{\partial f}{\partial \sigma_{ij}} = \left(\frac{\partial f}{\partial \sigma_m} \frac{\partial \sigma_m}{\partial \sigma_{ij}} + \frac{\partial f}{\partial \bar{\sigma}} \frac{\partial \bar{\sigma}}{\partial \sigma_{ij}} + \frac{\partial f}{\partial \theta} \frac{\partial \theta}{\partial \sigma_{ij}} \right) + \left(\frac{\partial f}{\partial \eta_f} \frac{\partial \eta_f}{\partial \sigma_{ij}} \right)$$

(2.54)

whereas

$$\frac{\partial \sigma_m}{\partial \sigma_{ij}} = -\frac{1}{3} \delta_{ij} \;\; ; \;\; \frac{\partial \bar{\sigma}}{\partial \sigma_{ij}} = \frac{1}{2\bar{\sigma}} s_{ij} \;\; ; \;\; \frac{\partial \theta}{\partial \sigma_{ij}} = \frac{\sqrt{3}}{2\bar{\sigma}^3 \cos 3\theta} \left(\frac{3 J_3}{2\bar{\sigma}^2} s_{ij} - s_{ik} s_{kj} + \frac{2}{3} \bar{\sigma}^2 \delta_{ij} \right)$$

(2.55)

The last term in equation (2.54) involves the anisotropy parameter and represents the influence of the loading orientation on plastic flow. Note that

$$\frac{\partial f}{\partial \eta_f} = -\frac{\vartheta(\kappa)}{\eta_f} g(\theta)(\sigma_m + C)$$

(2.56)

$$\frac{\partial \eta_f}{\partial \sigma_{ij}} = \frac{\partial \eta_f}{\partial \zeta} \frac{\partial \zeta}{\partial \sigma_{ij}} \;\; ; \;\; \zeta = A_{ij} l_i l_j = \frac{A_{ik} \sigma_{ij} \sigma_{kj}}{\sigma_{pq} \sigma_{pq}}$$

(2.57)

Considering equation (2.40) and differentiating yields

$$\frac{\partial \eta_f}{\partial \sigma_{ij}} = 2\hat{\eta}_f (1 + 2b_1 \zeta + 3b_2 \zeta^2 + ...) \frac{A_{ki} \sigma_{kj} \sigma_{pq} \sigma_{pq} - A_{pk} \sigma_{pq} \sigma_{kq} \sigma_{ij}}{(\sigma_{mn} \sigma_{mn})^2}$$

(2.58)

The gradient of the plastic potential function can be derived by using a similar procedure. The constitutive relation can now be obtained by invoking the additivity postulate. The general form is

$$d\varepsilon_{ij} = C_{ijkl}^{e} d\sigma_{kl} + d\varepsilon_{ij}^{p} = (C_{ijkl}^{e} + H_{p}^{-1} \frac{\partial f}{\partial \sigma_{ij}} \frac{\partial \psi}{\partial \sigma_{kl}}) d\sigma_{kl} = C_{ijkl} d\sigma_{kl} \tag{2.59}$$

Where C_{ijkl}^{e} is the elastic compliance matrix whose representation depends on the type of material anisotropy. In case of transverse isotropy, C_{ijkl}^{e} may be defined as

$$C = \begin{bmatrix} \dfrac{1}{E_2} & -\dfrac{\upsilon_{12}}{E_1} & -\dfrac{\upsilon_{12}}{E_1} & 0 & 0 & 0 \\[2mm] -\dfrac{\upsilon_{21}}{E_2} & \dfrac{1}{E_1} & -\dfrac{\upsilon_{13}}{E_1} & 0 & 0 & 0 \\[2mm] -\dfrac{\upsilon_{21}}{E_2} & -\dfrac{\upsilon_{13}}{E_1} & \dfrac{1}{E_1} & 0 & 0 & 0 \\[2mm] 0 & 0 & 0 & \dfrac{1}{G_{13}} & 0 & 0 \\[2mm] 0 & 0 & 0 & 0 & \dfrac{1}{G_{32}} & 0 \\[2mm] 0 & 0 & 0 & 0 & 0 & \dfrac{1}{G_{21}} \end{bmatrix} \tag{2.60}$$

Here, E_2 is the Young's modulus in the direction normal to the bedding plane, E_1 is the modulus in the plane of isotropy, υ_{ij} is the Poisson's ratio defining the deformation in j direction due to loading in i direction and G_{ij} is the shear modulus in (x_i, x_j) plane. It should be mentioned that G_{13} and υ_{21} are not independent and may be expressed as

$$G_{13} = \frac{E_1}{2(1+\upsilon_{13})} \quad ; \quad \frac{\upsilon_{21}}{E_2} = \frac{\upsilon_{12}}{E_1} \tag{2.61}$$

Thus, the representation (2.61) has only five independent parameters.

3.   Numerical integration of constitutive relations

3.1 Introduction

The elastoplastic constitutive relation for modeling the mechanical behaviour of Tournemire shale, which has been discussed in the previous chapter, represents a differential equation that cannot be reduced to a finite relation between stress and strain tensors, due to nonlinear/history dependent response. Therefore, for this class of constitutive models, a numerical integration is required. Numerical integration of incremental plasticity relations generally starts from a known state of stress, strain and internal plastic variables, at step n, i.e. $\{\sigma, \varepsilon, \alpha\}_n$. By satisfying the equilibrium and the constitutive relation, the corresponding stress/strain increments can be found. Using those values, the corresponding variables can be updated to $\{\sigma, \varepsilon, \alpha\}_{n+1}$ at step $n+1$. The available integration schemes can be divided into two main groups, namely, implicit and explicit. The most common explicit scheme is Forward-Euler (FE). The fully implicit or Backward-Euler (BE) and the midpoint-Euler (ME) are two commonly used implicit schemes. Consider the initial-value problem given by the differential equation

$$y = f(x) \ \rightarrow \ dy = df(x) \tag{3.62}$$

and assume the value of f to be known at time t. According to the Euler's scheme, for a small enough time increment Δt, there is a linear variation of function f within the time interval $[t, t + \Delta t]$. So the value of f at time step $t + \Delta t$ may be estimated as

$$f^{t+\Delta t} = f^t + \int_t^{t+\Delta t} \dot{f} dt = f^t + \dot{f} \Delta t = f^t + df \tag{3.63}$$

The general Euler's integration scheme, $f^{t+\Delta t}$ may be written as

21

$$f^{t+\Delta t} = f^t + \alpha \dot{f}^t \Delta t + (1-\alpha)\dot{f}^{t+\Delta t}\Delta t \ ; \ \alpha \in [0,1] \tag{3.64}$$

By assuming a particular value to coefficient α, various algorithms may be defined. The most common ones are

$\alpha = 1.0 \rightarrow$ explicit (Forward-Euler)

$\alpha = 0.5 \rightarrow$ implicit (midpoint-Euler)

$\alpha = 0.0 \rightarrow$ implicit (backward-Euler)

It should be mentioned that for the explicit scheme, the value of $f^{t+\Delta t}$ depends only on the known value of function f at time t, while for implicit scheme the value of f at $t + \Delta t$ is needed, which is unknown. So an iterative procedure is required.

As mentioned before, the microstructure tensor approach, which is used here for describing the anisotropic mechanical behavior of Tournemire shale, is based on Mohr-Coulomb failure criterion. Considering that the Mohr-Coulomb criterion is linear, the Forward-Euler scheme is chosen as a numerical integration scheme.

In analysing the initial boundary-value problems using finite element or finite difference methodologies, the basic unknowns are the displacement rates. The local strain rates that are determined from the kinematic relations are then used in the constitutive law for evaluating the stress rates. Thus, the integration algorithms should be written in strain-control regime.

In this chapter, point integration algorithms considering both implicit and explicit scheme are briefly presented. Later, the details of the explicit point integration methodology in relation to the microstructure tensor approach used for Tournemire shale are discussed.

3.2 Forward-Euler scheme

Applying the explicit (Forward-Euler) scheme, strain and stress at $t + \Delta t$ can be defined as

$$\varepsilon_{ij}^{t+\Delta t} = \varepsilon_{ij}^t + d\varepsilon_{ij}^t \tag{3.65}$$

$$
\begin{aligned}
\sigma_{ij}^{t+\Delta t} &= \sigma_{ij}^{t} + d\sigma_{ij}^{t} \\
&= \sigma_{ij}^{t} + D_{ijkl}(d\varepsilon_{ij}^{t} - d\varepsilon_{ij}^{pt}) \\
&= \sigma_{ij}^{t} + D_{ijkl}d\varepsilon_{ij}^{t} - D_{ijkl}\ d\lambda^{t}\ \frac{\partial \psi}{\partial \sigma_{ij}^{t}}
\end{aligned}
\tag{3.66}
$$

where

$$
d\varepsilon_{ij}^{p} = d\lambda\ \frac{\partial \psi}{\partial \sigma_{ij}}\ ;\quad \psi = \sqrt{3}\bar{\sigma} + \eta_{c}\ g(\theta)(\sigma_{m} + C)\ln\frac{(\sigma_{m} + C)}{\sigma_{m}^{0}} = 0
\tag{3.67}
$$

In the expressions above, D_{ijkl} is the elastic stiffness operator, ψ is the potential function defined in equation (3.67) and $d\lambda$ is an unknown plastic multiplier that may be identified by considering the consistency condition, $df = 0$, i.e.

$$
df^{t} = \frac{\partial f}{\partial \sigma_{ij}^{t}}d\sigma_{ij}^{t} + \frac{\partial f}{\partial \varepsilon_{q}^{pt}}d\varepsilon_{q}^{pt} = 0 \rightarrow \frac{\partial f}{\partial \sigma_{ij}^{t}}D_{ijkl}(d\varepsilon_{ij}^{t} - d\lambda^{t}\frac{\partial \psi}{\partial \sigma_{ij}^{t}}) + \frac{\partial f}{\partial \varepsilon_{q}^{pt}}d\lambda^{t}\frac{\partial \psi}{\partial q^{t}} = 0
\tag{3.68}
$$

Thus, $d\lambda$ can be evaluated as

$$
d\lambda^{t} = \frac{\dfrac{\partial f}{\partial \sigma_{ij}^{t}}D\ d\varepsilon_{ij}^{t}}{\dfrac{\partial f}{\partial \sigma_{ij}^{t}}D_{ijkl}\dfrac{\partial \psi}{\partial \sigma_{ij}^{t}} - \dfrac{\partial f}{\partial \varepsilon_{q}^{pt}}\dfrac{\partial \psi}{\partial q^{t}}} = (H_{e} + H_{p})^{-1}\frac{\partial f}{\partial \sigma_{ij}}D_{ijkl}d\varepsilon_{ij}
\tag{3.69}
$$

where

$$
H_{e} = \left(\frac{\partial f}{\partial \sigma_{ij}}(D_{ijkl}\frac{\partial \psi}{\partial \sigma_{kl}})\right);\quad H_{p} = -\left(\frac{\partial f}{\partial \varepsilon_{q}^{p}}\frac{\partial \psi}{\partial q}\right)
\tag{3.70}
$$

Given $d\lambda^{t}$, the updated $\sigma_{ij}^{t+\Delta t}$ may be determined and used as the initial value for the next step.

3.3 Backward-Euler scheme

For the implicit (Backward-Euler) scheme, the constitutive relation at $t + \Delta t$ can be written as

$$\varepsilon_{ij}^{t+\Delta t} = \varepsilon_{ij}^{t} + d\varepsilon_{ij}^{t+\Delta t} \tag{3.71}$$

$$\sigma_{ij}^{t+\Delta t} = \sigma_{ij}^{t} + D_{ijkl}(d\varepsilon_{ij} - d\varepsilon_{ij}^{p})^{t+\Delta t} = \sigma_{ij}^{t} + D_{ijkl}d\varepsilon_{ij}^{t+\Delta t} - D_{ijkl}\ d\lambda^{t+\Delta t}\ \frac{\partial \psi}{\partial \sigma_{ij}^{t+\Delta t}} \tag{3.72}$$

In equation (3.72) the values of both, $d\lambda$ and $\dfrac{\partial \psi}{\partial \sigma_{ij}}$ are evaluated at time step $t + \Delta t$, which

requires an iterative procedure. With reference to consistency condition, $f^{t+\Delta t}(\sigma_{ij}, \varepsilon_{q}^{p}) = 0$,

Maclaurin series is chosen for determining the value of $d\lambda$, and consequently σ_{ij} and $\dfrac{\partial \psi}{\partial \sigma_{ij}}$

, at each iteration. The details of the procedure are as follows:

$$f(d\lambda + \delta\lambda)^{i+1} = f^{i} + \left(\frac{\partial f}{\partial \lambda}\right)^{i} \delta\lambda^{i} = 0\ \rightarrow \delta\lambda^{i} = \frac{-f^{i}}{\left(\dfrac{\partial f}{\partial \lambda}\right)^{i}} \tag{3.73}$$

where

$$\frac{\partial f}{\partial \lambda} = \frac{\partial f}{\partial \sigma_{ij}}\frac{\partial \sigma_{ij}}{\partial \lambda} + \frac{\partial f}{\partial \varepsilon_{q}^{p}}\frac{\partial \varepsilon_{q}^{p}}{\partial \lambda} = -\left(\frac{\partial f}{\partial \sigma_{ij}}(D_{ijkl}\frac{\partial \psi}{\partial \sigma_{kl}})\right) + \left(\frac{\partial f}{\partial \varepsilon_{q}^{p}}\frac{\partial \psi}{\partial q}\right) = -(H_{e} + H_{p}) \tag{3.74}$$

Thus,

$$\delta\lambda^{i} = \left(\frac{f}{H_{e} + H_{p}}\right)^{i} \tag{3.75}$$

$$d\lambda^{i+1} = d\lambda^{i} + \delta\lambda^{i} \tag{3.76}$$

24

$$d\sigma_{ij}^{i+1} = D_{ijkl}\left(d\varepsilon_{kl}^i - d\lambda^{i+1}(\frac{\partial\psi}{\partial\sigma_{kl}})^i\right)$$
(3.77)

$$\left(\sigma_{ij}^{t+\Delta t}\right)^{i+1} = \sigma_{ij}^t + \left(d\sigma_{ij}\right)^{i+1}$$
(3.78)

The procedure has to be repeated until $d\lambda^{i+1} \cong d\lambda^i$ within an acceptable range of error is reached, or in other words, $\delta\lambda^i \cong 0$. Given $d\lambda^{t+\Delta t}$, the stress at $t + \Delta t$, represented by $\sigma_{ij}^{t+\Delta t}$, may be determined. This can be used as the initial value for the next increment.

3.4   Explicit integration algorithm (strain-controlled) incorporating microstructure tensor for Tournemire shale

Considering $d\varepsilon_{ij}$ as a known parameter, and also knowing stress and strain at each time step, t, the algorithm below may be used to calculate the stress at time $t + \Delta t$.

The first step is to compute the plastic multiplier. It should be pointed out again that, in order to simplify the algebra, the components of strain and the stress tensors can be referred to the coordinate system associated with the principal material axes. Their values can then be transformed to the global frame of reference using the standard transformation rules. For completeness, let us first review the key governing equations. The loading surface is expressed as

$$f = \sqrt{3}\bar{\sigma} - \vartheta g(\theta)\left(\sigma_m + C\right) = 0$$

where

$$g(\theta) = \frac{3 - \sin\phi}{2\sqrt{3}\cos\theta - 2\sin\theta\sin\phi} \quad ; \quad \theta = \frac{1}{3}\sin^{-1}\left(\frac{-3\sqrt{3}}{2}\frac{J_3}{\bar{\sigma}^3}\right) \quad \wedge \quad -\frac{\pi}{6} \leq \theta \leq \frac{\pi}{6}$$

$$\bar{\sigma} = (J_2)^{\frac{1}{2}} \; ; \quad \sigma_m = -\frac{1}{3} I_1$$

and ϑ is the hardening parameter defined as

$$\vartheta = \eta_f \frac{\varepsilon_q^p}{A + \varepsilon_q^p}$$

The expression for the anisotropy parameter η_f takes the form

$$\eta_f = \eta_{f_0} \left(1 + \xi + b_1 \xi^2 + b_2 \xi^3 + ... \right); \quad \xi = A_{ij} l_i l_j = A_1 l_1^2 + A_2 l_2^2 + A_3 l_3^2$$

where l_1^2, l_2^2 and l_3^2 are unit vectors along the loading direction referred to the principal material axes coordinates (equation (2.45)).

Since the response of Tournemire shale is transversely isotropic, the expression for η_f may be reduced to

$$\eta_f = \eta_{f_0} \left(1 + A_1 (1 - 3l_2^2) + b_1 A_1^2 (1 - 3l_2^2)^2 + b_2 A_1^3 (1 - 3l_2^2)^3 + ... \right)$$

The plastic potential function is defined as

$$\psi = \sqrt{3}\bar{\sigma} + \eta_c \, g(\theta)(\sigma_m + C) \ln \frac{(\sigma_m + C)}{\sigma_m^0} = 0 \; ; \; \eta_c = \alpha \eta_f$$

where, σ_m^0 and η_c are constants.

Applying the consistency condition, $df = 0$, yields

$$d\lambda^t = (H_e^t + H_p^t)^{-1} \frac{\partial f}{\partial \sigma_{ij}^t} D_{ijkl} d\varepsilon_{ij}^t = \frac{\dfrac{\partial f}{\partial \sigma_{ij}^t} D_{ijkl} \, d\varepsilon_{ij}^t}{\dfrac{\partial f}{\partial \sigma_{ij}^t} D_{ijkl} \dfrac{\partial \psi}{\partial \sigma_{ij}^t} - \dfrac{\partial f}{\partial \varepsilon_q^{pt}} \dfrac{\partial \psi}{\partial q^t}}$$

in which

$$\frac{\partial f}{\partial \sigma_{ij}^t} = \left(\frac{\partial f}{\partial \sigma_m^t} \frac{\partial \sigma_m^t}{\partial \sigma_{ij}^t} + \frac{\partial f}{\partial \bar{\sigma}^t} \frac{\partial \bar{\sigma}^t}{\partial \sigma_{ij}^t} + \frac{\partial f}{\partial \theta^t} \frac{\partial \theta^t}{\partial \sigma_{ij}^t} \right) + \left(\frac{\partial f}{\partial \eta_f^t} \frac{\partial \eta_f^t}{\partial \sigma_{ij}^t} \right)$$

The derivatives appearing in the expression above take the following form

$$\frac{\partial f}{\partial \sigma_m^t} = -\vartheta^t g(\theta) \;;\quad \frac{\partial \sigma_m^t}{\partial \sigma_{ij}^t} = -\frac{1}{3} \delta_{ij}$$

$$\frac{\partial f}{\partial \bar{\sigma}^t} = \sqrt{3} \;;\quad \frac{\partial \bar{\sigma}^t}{\partial \sigma_{ij}^t} = \frac{1}{2\bar{\sigma}^t} s_{ij}^t$$

$$\frac{\partial f}{\partial \theta^t} = \frac{\partial f}{\partial g(\theta)} \frac{\partial g(\theta)}{\partial \theta^t} = \left(-\vartheta^t (\sigma_m^t + C)\right) \left(\frac{2\sqrt{3} \sin(\theta) + 2\cos(\theta)\sin(\phi)(3 - \sin(\phi))}{(2\sqrt{3} \cos(\theta) - 2\sin(\theta)\sin(\phi))^2} \right)$$

$$\frac{\partial \theta^t}{\partial \sigma_{ij}^t} = \frac{\sqrt{3}}{2\bar{\sigma}^{3t} \cos 3\theta} \left(\frac{3J_3}{2\bar{\sigma}^2} s_{ij}^t - s_{ik}^t s_{kj}^t + \frac{2}{3} \bar{\sigma}^{2t} \delta_{ij} \right)$$

$$\frac{\partial f}{\partial \eta_f^t} = -g(\theta)^t \left(\sigma_m^t + C \right) \frac{\varepsilon_q^{pt}}{B + \varepsilon_q^{pt}}$$

$$\frac{\partial \eta_f^t}{\partial \sigma_{ij}^t} = \frac{\partial \eta_f^t}{\partial \xi^t} \frac{\partial \xi^t}{\partial \sigma_{ij}^t} = \eta_{f_0} \left(1 + 2b_1\xi + 3b_2\xi^2 + ... \right)^t \frac{\partial \xi^t}{\partial \sigma_{ij}^t}$$

$$\frac{\partial \xi^t}{\partial \sigma_{ij}^t} = 2A_1 l_1^t \frac{\partial l_1^t}{\partial \sigma_{ij}^t} + 2A_2 l_2 \frac{\partial l_2^t}{\partial \sigma_{ij}^t} + 2A_3 l_3 \frac{\partial l_3^t}{\partial \sigma_{ij}^t}$$

In the next step, the plastic strain and the deviatoric plastic strain increments have to be evaluated and all variables should be updated. Thus,

$$\left(d\varepsilon_{ij}^{p}\right)^{t} = d\lambda^{t}\frac{\partial\psi}{\partial\sigma_{ij}^{t}}$$

$$\sigma_{ij}^{t+\Delta t} = \sigma_{ij}^{t} + d\sigma_{ij}^{t} = \sigma_{ij}^{t} + D_{ijkl}(d\varepsilon_{ij}^{t} - d\varepsilon_{ij}^{pt})$$
$$= \sigma_{ij}^{t} + D_{ijkl}d\varepsilon_{ij}^{t} - D_{ijkl}\ d\lambda^{t}\ \frac{\partial\psi}{\partial\sigma_{ij}^{t}}$$

$$d\varepsilon_{q}^{pt} = d\lambda^{t}\frac{\partial\psi}{\partial q^{t}}$$

$$\left(\varepsilon_{q}^{p}\right)^{t+\Delta t} = \left(\varepsilon_{q}^{p}\right)^{t} + \left(d\varepsilon_{q}^{p}\right)^{t}$$

Moreover, in order to use the formulation as the constitutive model in finite element, the tangential stiffness operator $\bar{D}_{ijkl}$ must be calculated, as

$$\sigma_{ij}^{t+\Delta t} = \sigma_{ij}^{t} + d\sigma_{ij}^{t} = \sigma_{ij}^{t} + D_{ijkl}(d\varepsilon_{ij}^{t} - d\varepsilon_{ij}^{pt})$$
$$= \sigma_{ij}^{t} + \bar{D}_{ijkl}\ d\varepsilon_{kl}^{t}$$

$$\bar{D}_{ijkl} = D_{ijkl} - \frac{D_{ijmn}\dfrac{\partial\psi}{\partial\sigma_{mn}^{t}}\dfrac{\partial f}{\partial\sigma_{pq}^{t}}D_{pqkl}}{\dfrac{\partial f}{\partial\sigma_{rs}^{t}}D_{rstu}\ \dfrac{\partial\psi}{\partial\sigma_{tu}^{t}} - \dfrac{\partial f}{\partial\varepsilon_{q}^{pt}}\dfrac{\partial\psi}{\partial q^{t}}}$$

This finalizes the constitutive model that can be used in FEM packages.

4.   Identification of parameters and verification of the model

4.1 Identification of material parameters

The framework outlined in the second chapter, third section, requires specification of several parameters including strength descriptors associated with the failure criterion, coefficients of best-fit approximation governing their distribution and the hardening parameters. Let's consider the Mohr-Coulomb failure criterion in *p-q* space,

$$F = q - \vartheta(p + C) = 0 \tag{4.79}$$

where ϑ is a hardening function which is defined in equation (2.50) and *C=const.* is a strength parameter. The stress measures *p* and *q* may are defined in the form

$$q = \sigma_1 - \sigma_3 \;\; ; \;\; p = \frac{\sigma_1 + 2\sigma_3}{3} = P_0 + \frac{q}{3} \tag{4.80}$$

Here, σ_1 is the major principal stress and $\sigma_2 = \sigma_3 = P_0$ are the minor principal stresses. In order to identify ϑ and C a series of triaxial tests is required. For this purpose, experimental results at different initial confining pressure, performed by Niandou et al. (1997), are employed. The material tested is a shale taken from Tournemire site in the Massif Central, France. The mechanical behavior is transversely isotropic due to existence of bedding planes. Table 4. 1 shows the mineralogical composition of this type of shale, while Figure 4. 1 shows the variation of axial strength versus orientation of bedding planes.

Table 4. 1 The mineralogical composition of the Tournemire shale (H. Niandou et al., 1997)

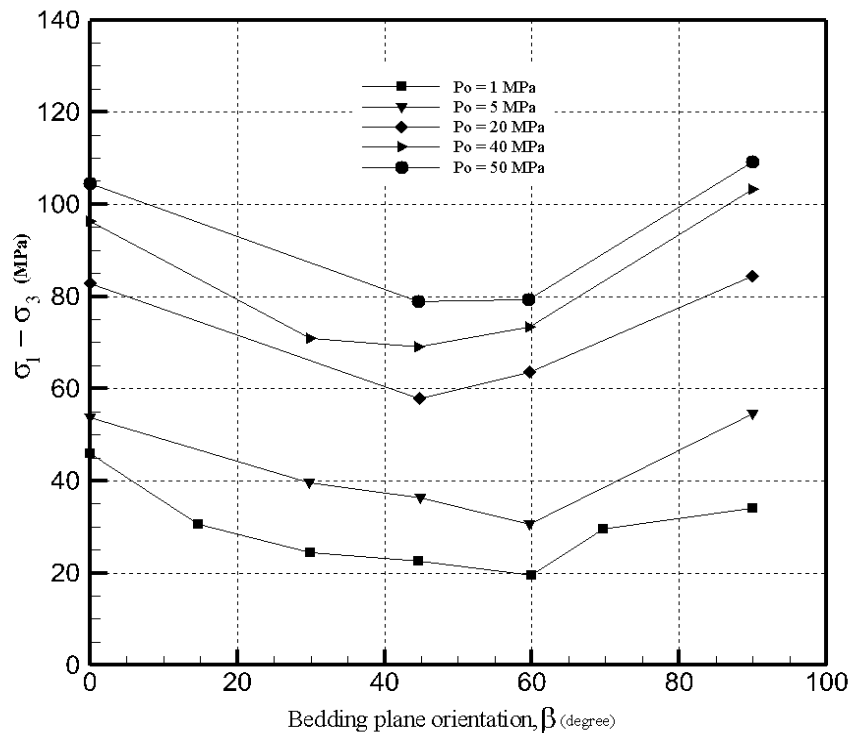| Minerals	Weight Proportion (%)
Kaolinite	27.5%
Illite	16.5%
Quartz	19%
Calcite	15%
Chlorite	2.7%
Interstratifier	8.3%
Other minerals	11%
Water	4.5% - 8%

Figure 4. 3 variation of deviatoric stress at failure vs. orientation of bedding planes for various confining pressures (H. Niandou et al., 1997)

Failure surface in $p-q$ plane for different orientations can be drawn by considering the deviatoric stress, q, at failure for different initial pressures and calculating the corresponding mean stress, p. The Mohr-Coulomb failure line can be created by best fit approximation of these points. Then, the C parameter may be determined by dividing the intercept of each line by the slope of it. As C must be constant and invariant with respect to orientation, an average value of $1.2E+01$ MPa has been selected. Now ϑ at different initial pressures and different orientation of bedding planes can be evaluated as

$$\vartheta = \frac{q}{(p+C)} \tag{4.81}$$

It should be stressed here that the identification is based on tests involving low initial confining pressures only $(P_0 = 1, 5, 20 \ MPa)$, which is due to the fact that the linear form of Mohr-Coulomb criterion cannot adequately describe the response at higher pressures. The latter requires a non-linear form of the failure criterion. Figure 4. 4 and Figure 4. 5 show the failure envelopes in $p-q$ space for $\beta = 30$ and 45 degrees, respectively. The rest of the $p-q$ data, also the resultant C and ϑ values, are summarized in Table 4. 2 through Table 4. 4. It should be restated that when $\kappa \rightarrow \infty$ there is $f \rightarrow F$ and $\vartheta \rightarrow \eta_f$. As can be seen from the data, the C parameter for $\beta = 90$ degrees is out of range. So it is not considered in identifying the average value of the parameter C value.
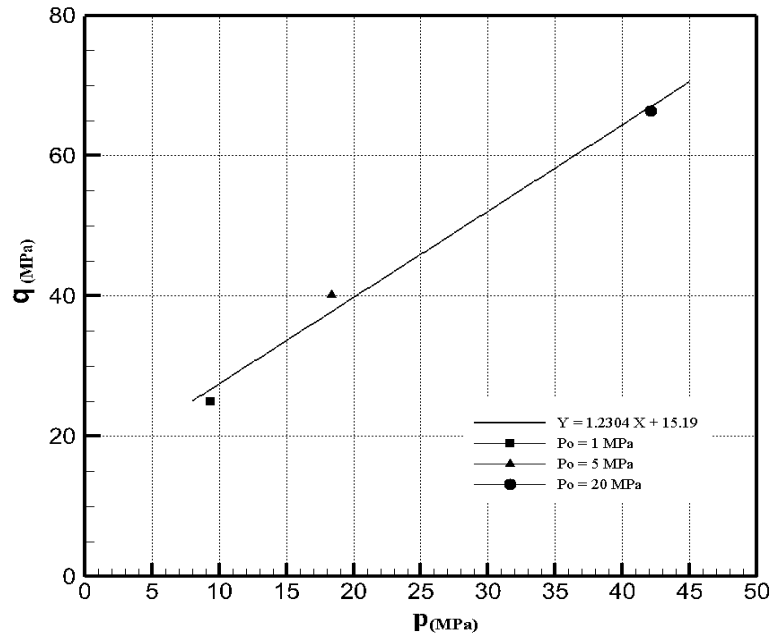
Figure 4. 4 Variation of deviatoric stress vs. the mean stress at failure for different values of initial pressure at $\beta = 30°$
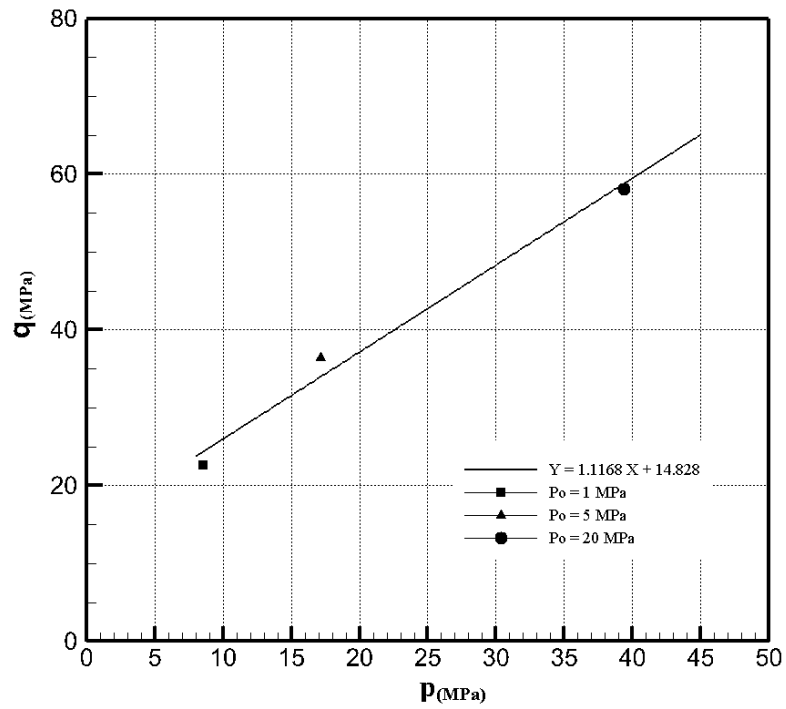

Figure 4. 5 Variation of deviatoric stress vs. the mean stress at failure for different values of initial pressure at $\beta = 45°$

Table 4. 2 *Mohr-Coulomb failure* envelope data for $\beta = 0°, 20°$

	$\beta = 0°$			$\beta = 20°$		
$P_0(MPa)$	1	5	20	1	5	20
q (MPa)	4.602E+01	5.365E+01	8.277E+01	2.877E+01	4.487E+01	7.162E+01
P (MPa)	1.634E+01	2.288E+01	4.759E+01	1.059E+01	1.996E+01	4.387E+01
C (MPa)	1.447E+01			1.244E+01		
η_f	1.623E+00	1.537E+00	1.389E+00	1.273E+00	1.403E+00	1.282E+00

Table 4. 3 *Mohr-Coulomb failure envelope* data for $\beta = 60°, 70°$

	$\beta = 60°$			$\beta = 70°$		
$P_0(MPa)$	1	5	20	1	5	20
q (MPa)	2.000E+01	3.131E+01	6.389E+01	2.937E+01	3.890E+01	7.155E+01
P (MPa)	7.666E+00	1.544E+01	4.130E+01	1.079E+01	1.797E+01	4.385E+01
C (MPa)	1.235E+01			1.380E+01		
η_f	1.016E+00	1.141E+00	1.198E+00	1.288E+00	1.297E+00	1.281E+00

Table 4. 4 *Mohr-Coulomb failure envelope* data for $\beta = 90°$

$\beta = 90°$			
$P_0 (MPa)$	1	5	20
$q (MPa)$	3.471E+01	5.507E+01	8.493E+01
$P (MPa)$	1.257E+01	2.336E+01	4.831E+01
$C (MPa)$	2.274E+01		
η_f	1.412E+00	1.557E+00	1.408E+00

Figure 4. 6 shows anisotropy parameter variation as a function of bedding plane orientation corresponding to various confining pressures.
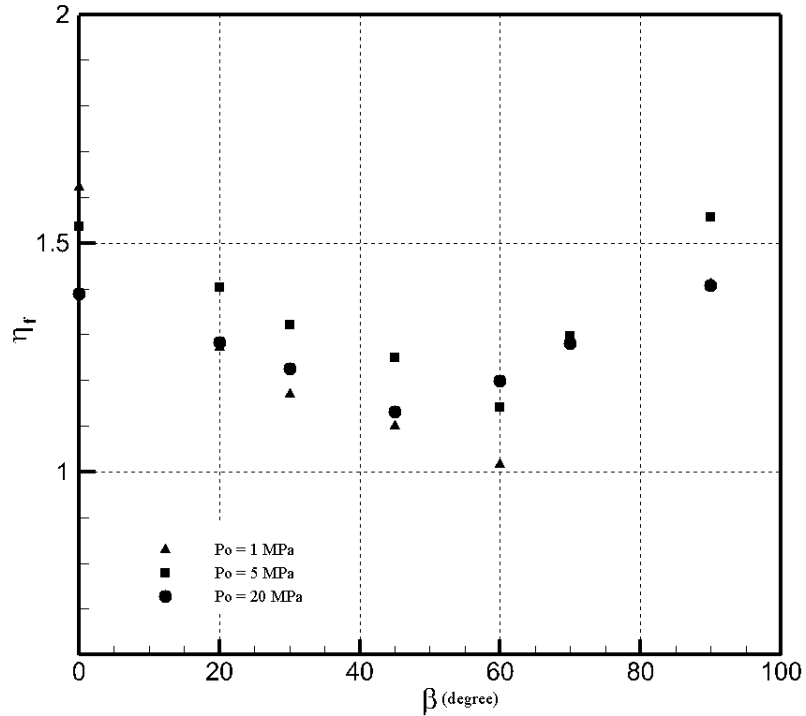
Figure 4. 6 Variation of η_f vs. orientation of bedding planes for various confining pressures

Evidently, the results indicate that the maximum strengths is associated with specimens in which the direction of major principal stress is either parallel or perpendicular to the bedding planes, while the minimum strength has been observed for orientations between 30 and 60 degrees.

The next step is to calculate the coefficients $(\eta_{f_0}, A_1, b_1, b_2, ...)$ which appear in the anisotropy parameter. With reference to chapter two, the anisotropy parameter can be written as

$$\eta_f = \eta_{f_0}\left(1 + A_1\zeta + b_1 A_1^2 \zeta^2 + b_2 A_1^3 \zeta^3 + ...\right) \tag{4.82}$$

where

$$\zeta = (1 - 3l_2^2) \quad ; \quad l_2^2 = \frac{P_0^2 \sin^2 \beta + \sigma_1^2 \cos^2 \beta}{2P_0^2 + \sigma_1^2} \tag{4.83}$$

For triaxial tests, ξ can be identified simply by substituting P_0 and σ_1 at failure corresponding to each bedding plane orientation. So, by knowing η_f and ξ for different orientation and initial pressure, the $\eta_f - \xi$ diagram can be drawn. Figure 4. 7 shows the best fit approximation based on equation (4.82), which incorporates second order term. The corresponding values of the coefficients of approximation are as follows,

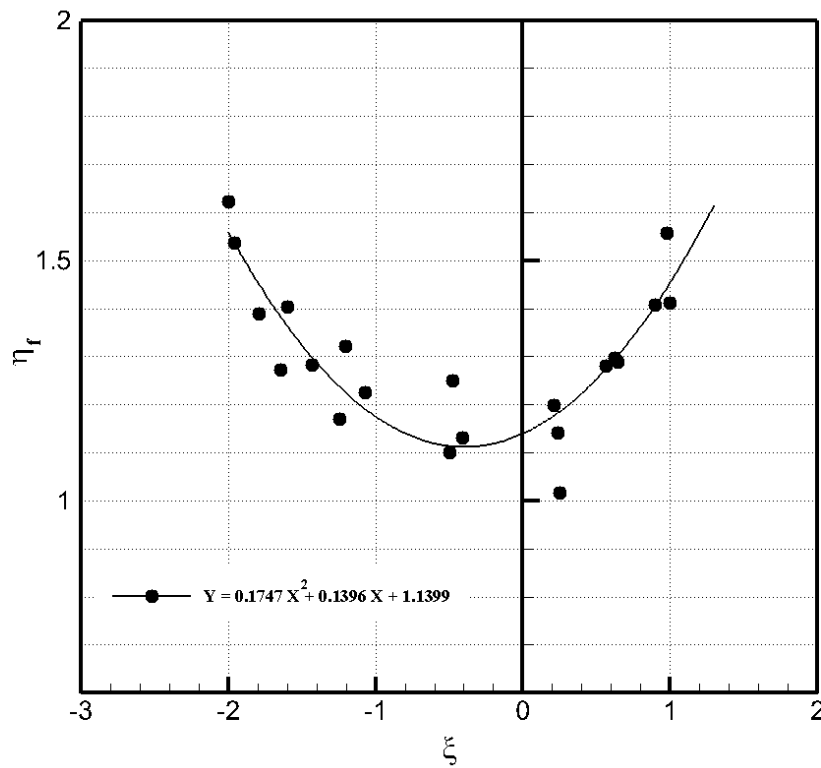$$\eta_{f_0} = 1.14 \,, \ A_1 = 0.122 \,, \ b_1 = 10.22$$

Figure 4. 7 variation of η_f vs. ζ

The next issue is to identify the material constant, A, which appears in the hardening parameter, $\vartheta(\kappa)$, i.e.

$$\vartheta = \vartheta(\kappa) = \eta_f \frac{\kappa}{A+\kappa} \quad ; \quad \kappa = \varepsilon_q^p \tag{4.84}$$

where κ is deviatoric plastic strain. As can be seen from this equation, the plastic strain must be quantified in order to be able to identify the value for *A*. The plastic strain can be extracted from the available total strain by defining the elastic response. The latter can be estimated by using the elastic material properties evaluated from unloading curves. Elastic constants for Tournemire shale were estimated here based on the work of Halidou et al. (1994) and are as follows,

$$E_1 = 22000 \ MPa; \ E_2 = 7000 MPa; \ \upsilon_{21} = 0.12; \ \upsilon_{13} = 0.14; \ G = 4000 MPa$$

Here, E_1 is the Young's modulus in the direction tangential to the bedding plane, E_2 is the Young's modulus in the direction normal to the bedding plane, while υ_{ij} is the Poisson's ratio that defines deformation in the X_j direction due to normal stress in the X_i direction. Once the total and elastic strains are defined, the equivalent (distortional) strain, ε_q and ε_q^e, can be determined. Then, the equivalent plastic strain, ε_q^p or κ, may be calculated as a difference between the total and elastic equivalent strain. Then, by plotting $\dfrac{\vartheta}{\eta_f}$ against ε_q^p, equivalent plastic strain, and performing the curve-fitting, the *A* parameter can be identified. It should be noted that since the material is transversely isotropic, traditional triaxial measurements (i.e. axial and volumetric strains) are, in general, not sufficient. In fact, for the inclined samples, shearing deformations as well as out of plane deformations will develop, which play an important role in estimation of the equivalent plastic strain. Thus, in Niandou et al. (1997) experiments , only the tests on horizontal samples provide reliable measures of plastic deformation. Therefore, the *A* parameter has been identified here from these measurements alone and then calibrated using numerical simulation for other orientations, by matching the axial deformation-deviatoric stress curves.

The key assumptions adopted here for constructing the $\varepsilon_p^q - \dfrac{\vartheta}{\eta_f}$ diagram, and for obtaining the best fit approximation, as shown in Figure 4. 8, are listed below

1) Since the approximation of conditions at failure is based on a linear representation, the tests at high confinements, viz. $\sigma_3 = 30$ and $50MPa$, are not considered.

2) The results shown in Figure 4. 8, show that the initial part of the initial portion of the deviatoric characteristic shows a concavity, which is not typical. This may be due to closure of some fractures which might have been present within the sample at the start of axial loading. Thus, the points up to $\dfrac{\vartheta}{\eta_f} = 0.4$ have been disregarded in performing the curve-fitting.

3) The experimental data indicate that the failure is not associated with unlimited deformation, but there is an abrupt transition to localized deformation. In order to account for this, another coefficient B has been incorporated in the hardening function, viz.

$$\frac{\vartheta}{\eta_f} = B\frac{\kappa}{A+\kappa} \quad ; \quad \kappa = \varepsilon_q^p \tag{4.85}$$

The best-fit approximation, Figure 4.6, resulted in the following values

$$A = 0.\,0027; \; B = 1.28$$

Since A and B are defined only based on horizontal bedding plane, it is expected not to get accurate deformation responses for other oriented samples. One way that this issue can be addressed is by conducting numerical simulations for other orientations of the bedding planes and comparing the response with experimental data. This will results in modified valued for A and B that can reproduce the experimental data more accurately for all orientations. Following this approach, A and B may be modified to
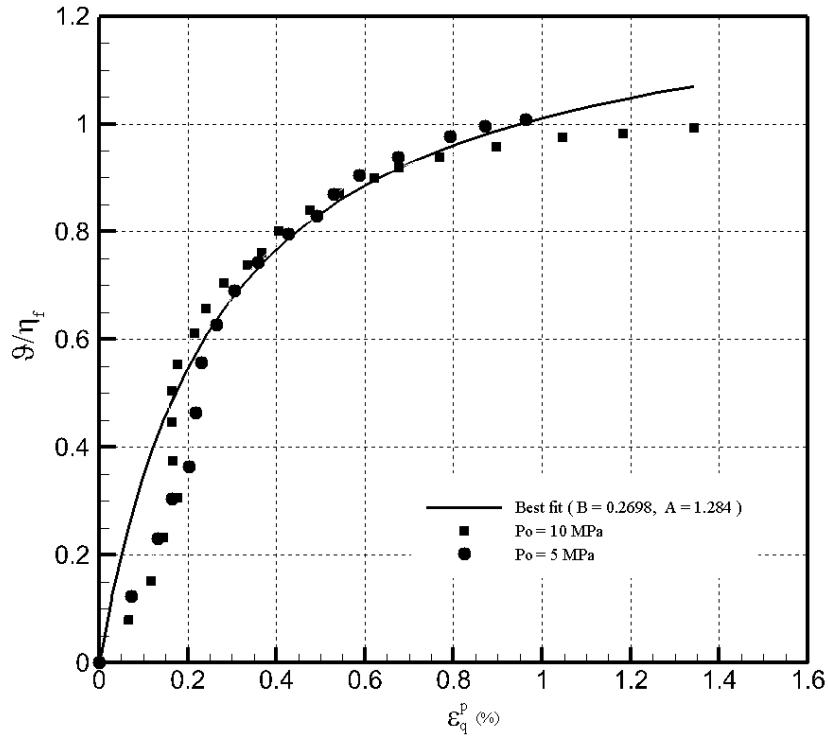
$$A = 0.001; \; B = 1.1$$

Figure 4. 8 ε_p^q vs. ϑ / η_f curves for different confining pressure and the resulting curve-fitting

The next step is to specify the parameter, η_c, which appears in the plastic potential function as defined in equation (2.52). This parameter is a constant that describes the transition from plastic compaction to dilatancy before failure, where there is $d\varepsilon_v^p = d\lambda \dfrac{\partial \psi}{\partial p} = 0 \rightarrow$

$\dfrac{\partial \psi}{\partial p} = 0$. Thus, its value defines the slope of zero dilatancy line $\eta_c = \vartheta$. The details of the identification of η_c are provided below.

The plastic potential function in equation (2.51) can be rewritten in p-q space as

$$\psi = q + \eta_c (p + C) \ln(\frac{p + C}{\bar{p}}) = 0 \tag{4.86}$$

Where $\overline{p}$ is a constant that can be obtained by considering the condition of $\psi(p,q) = 0$. Also, according to equation (4.86), there is

$$\frac{\partial \psi}{\partial p} = \eta_c \left(\ln \frac{p+C}{\overline{p}} + 1 \right) = \eta_c - \vartheta \tag{4.87}$$

So that $\vartheta = \dfrac{q}{p+C} = \eta_c \rightarrow \dfrac{\partial \psi}{\partial p} = 0 \rightarrow d\varepsilon_v^p = 0$, which defines the transition from compaction to dilatancy. Consequently, the value of η_c may be determined by plotting the $\vartheta - \varepsilon_v^p$ diagram Figure 4. 7. For the locus where $d\varepsilon_v^p = 0$, $\vartheta = \eta_c$. Obviously, for $\vartheta < \eta_c$ there is compaction whereas, $\eta_c < \vartheta$ corresponds to dilation.
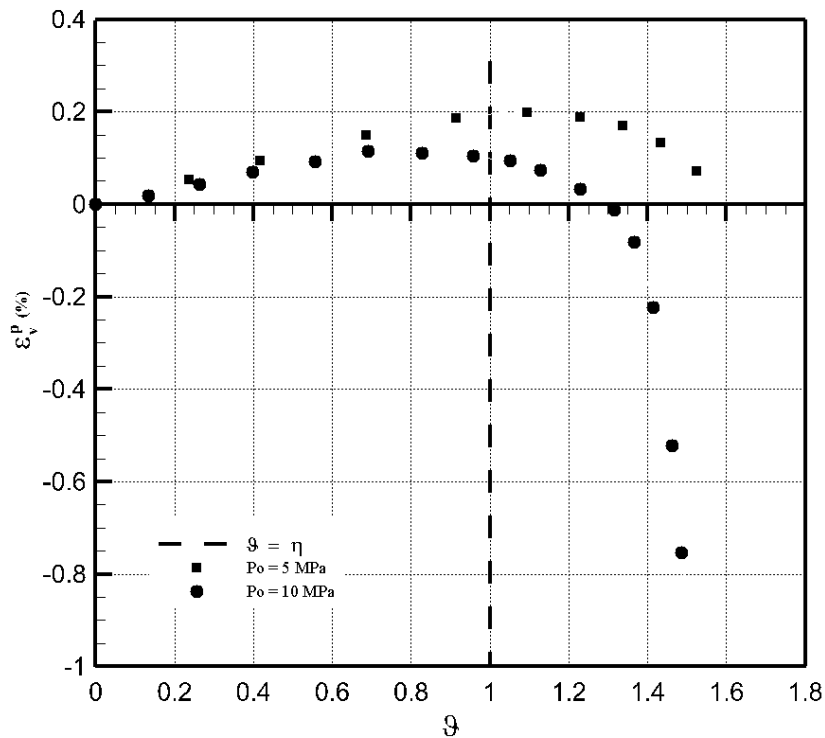

Figure 4. 7 ε_v^p vs. ϑ variation (evolution of volume change)

4.2   Model verification through numerical simulations

After identifying basic material parameters which are needed in applying the microstructure tensor formulation, the numerical simulations for other loading histories are required in order to verify the performance of the model. For this purpose the results of a number of triaxial tests reported by Niandou et al. (1997) are chosen . As mentioned before, tests were carried out on Tournemire shale at various initial confining pressures and orientations of the bedding planes.

A set of numerical predictions and experimental data for triaxial compression tests with confining pressures ranging from 5 to 30 *MPa*, and bedding planes orientations equal to 0, 45, and 90 degrees are presented in Figure 4. 8 to Figure 4. 13. Comparisons between numerical simulation and experimental results show that the model is capable of reproducing the main features in the mechanical response of the transversely isotropic Tournemire shale. For example, the fact that the mechanical strength increases and plastic deformation becomes more noticeable under higher confining pressure. The transition from volumetric compaction to dilatancy is also well reproduced. However, it seems that a quadratic form of the failure function may be more adequate to reproduce the mechanical behavior of Tournemire shale at higher confining pressures. Moreover, it is noted that the strain softening associated with strain localization takes place under lower confining pressures. Since the formulation discussed here is limited to the strain hardening range, the numerical simulations were stopped at the point where $\dfrac{\eta}{\eta_f} \leq 0.98$. The strain softening part of experimental results taken from the research of H. Niandou et al., (1997) is also omitted as it should be considered as a boundary-value problem.

Figure 4. 8 to Figure 4. 10 show the mechanical response of samples loaded in the direction normal to the bedding planes, i.e. $\beta = 0$ degrees and confining pressures of 5, 10, and 30 *MPa* respectively. Figure 4. 8a, Figure 4. 9a and Figure 4. 10 show the deviatoric stress

against axial deformation. It is obvious that the ultimate strength is considerably affected by the confining pressure.

Figure 4. 8b and Figure 4. 9b present the deviatoric stress against volume change characteristics. It should be noted that for $P_0 = 30\ MPa$, the $q - \varepsilon_v$ diagram is not shown as there is no experimental information available. It can be seen that the samples go through progressive compaction before the conditions at failure are reached.

Figure 4. 11 shows the mechanical response of inclined samples with bedding planes orientation of $\beta = 45$ degrees and confining pressure of 5 MPa. Here, the simulation is not quite consistent with the experimental data. However, it should be pointed out again that for inclined samples the deformation is no longer axisymmetric and the experimental results should be taken with caution. In general, the axial strength at failure and the corresponding axial strain is significantly lower compared to those for samples tested at $\beta = 0$ degree. For instance, the axial strain corresponding to peak deviatoric stress is about 1.8% for $\beta = 0$ degrees, while the axial strain for $\beta = 45$ degrees corresponding to peak stress (37 MPa) is 0.85%. These resultants indicate a significant effect of anisotropy on both the failure stress and the plastic deformation.

Finally, the comparisons of simulations and the results of triaxial compression tests at $\beta = 90$ degrees are presented in Figure 4. 12 and Figure 4. 13. The results correspond to confining pressures of $5MPa$ and $30MPa$ respectively. It can be seen that the strength of these samples is higher compared to the samples tested at $\beta = 45$ degrees. Also, the volumetric dilatancy becomes more noticeable, probably because of the opening of the foliation in this direction. It should again be noted that there is no experimental data available on volumetric strain for the vertical samples tested at $P_0 = 30\ MPa$
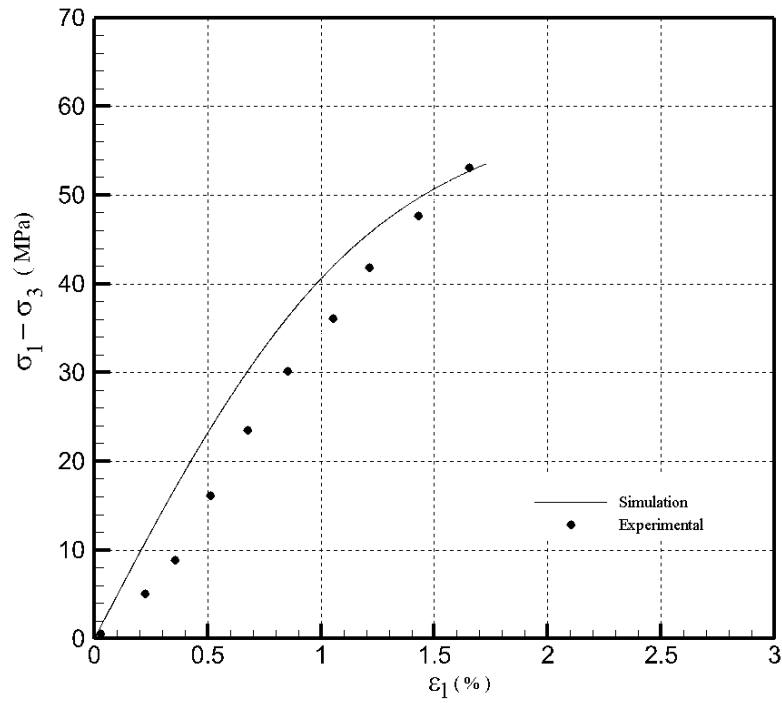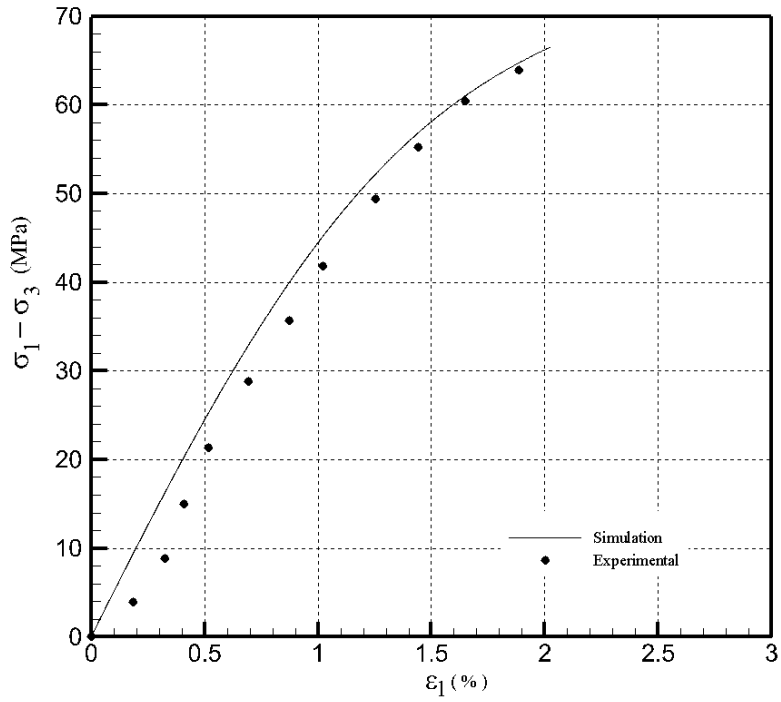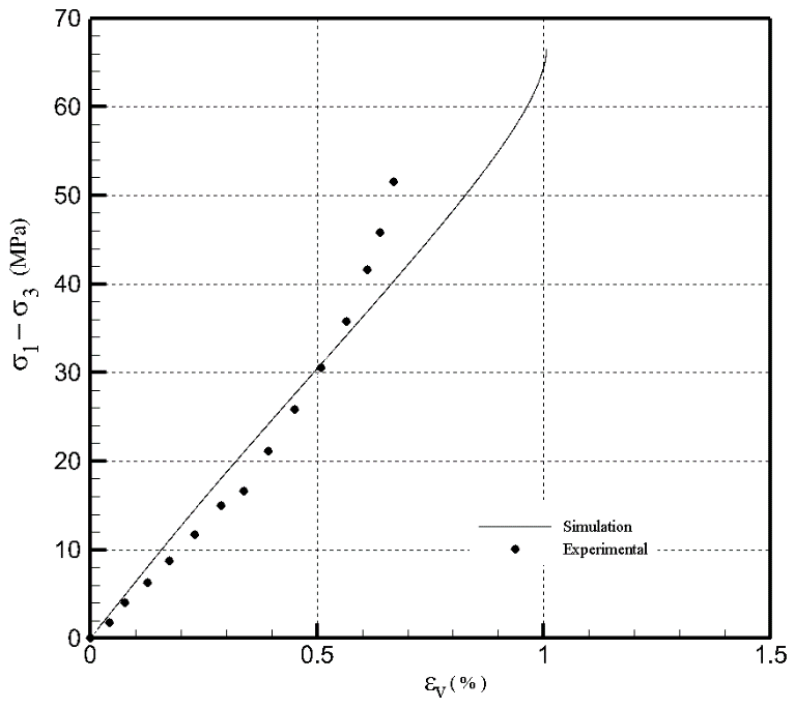
(a)
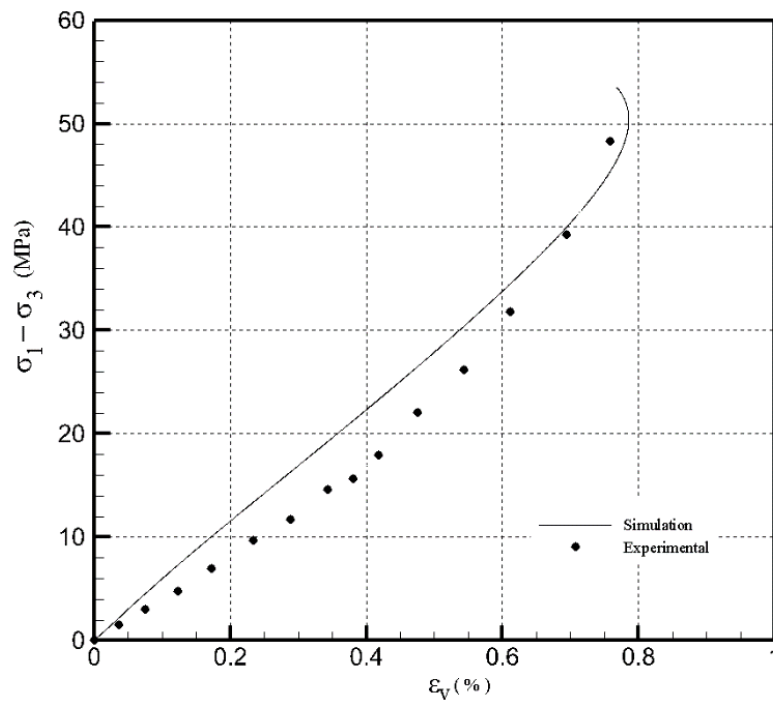
(b)

Figure 4. 8 numerical results of compression triaxial tests for horizontal bedding planes, $\beta = 0$, at $P_0 =$ 5MPa; (a) deviatoric stress versus axial strain and (b) volumetric strain, $\varepsilon_v = - (\varepsilon_x + \varepsilon_y + \varepsilon_z)$

(a)

(b)

Figure 4. 9 numerical results of compression triaxial tests for horizontal bedding planes, $\beta = 0$, at $P_0 = 10$ MPa; (a) deviatoric stress versus axial strain and (b) volumetric strain, $\varepsilon_v = - (\varepsilon_x + \varepsilon_y + \varepsilon_z)$.
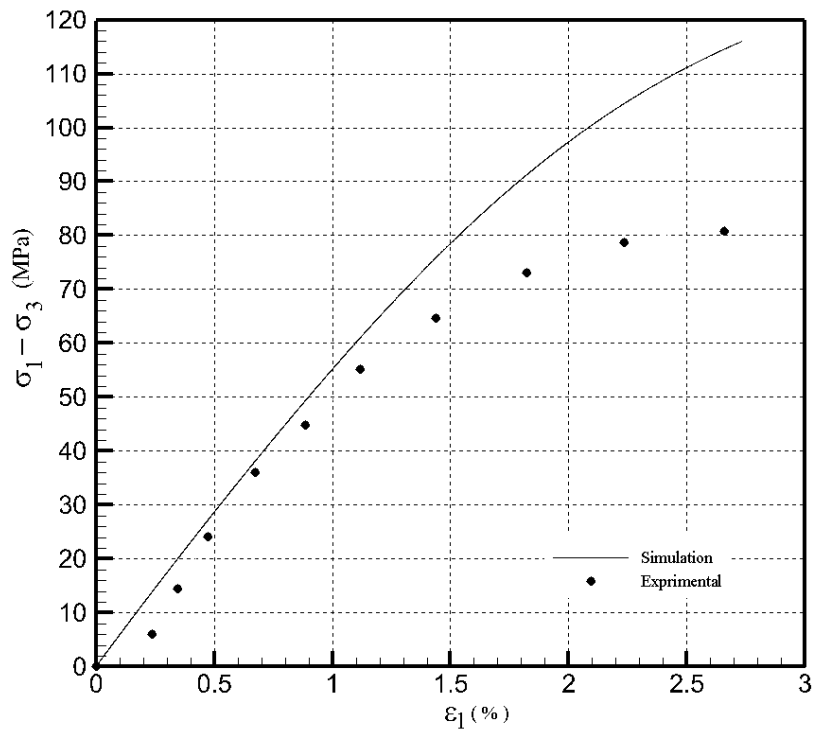
Figure 4. 10 Numerical simulation of triaxial tests (deviatoric stress versus axial strain for horizontal bedding planes, $\beta = 0$, at $P_0 = 30$ MPa)

(a)

(b)

Figure 4. 11 Numerical results of compression triaxial tests for horizontal bedding planes, $\beta = 45°$, at $P_0 = 5$ MPa; (a) deviatoric stress versus axial strain and (b) volumetric strain, $\varepsilon_v = - (\varepsilon_x + \varepsilon_y + \varepsilon_z)$.

(a)

(b)

Figure 4. 12 Numerical results of compression triaxial tests for vertical bedding planes, $\beta = 90^\circ$, at P0 = 5 MPa; (a) deviatoric stress versus axial strain and (b) volumetric strain, $\varepsilon v = - (\varepsilon_x + \varepsilon_y + \varepsilon_z)$.
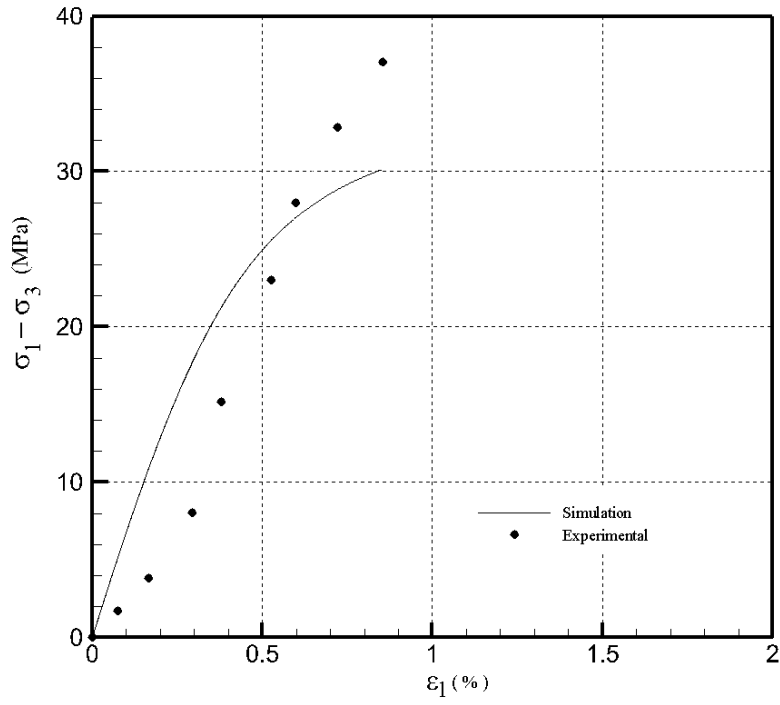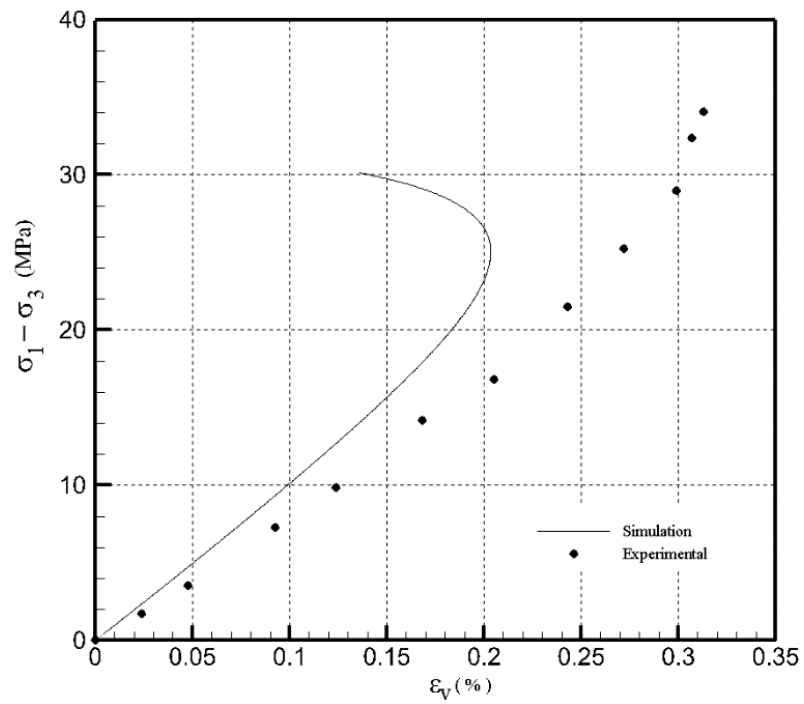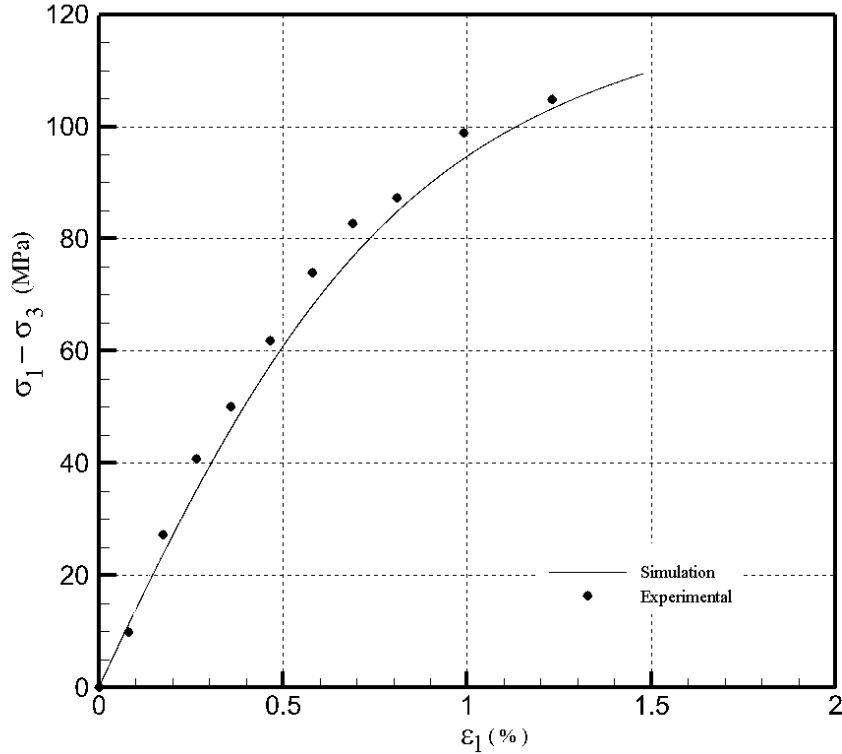
Figure 4. 13 Numerical simulation of triaxial tests (deviatoric stress versus axial strain for horizontal bedding planes, $\beta = 90°$, at $P_0 = 30$ MPa)
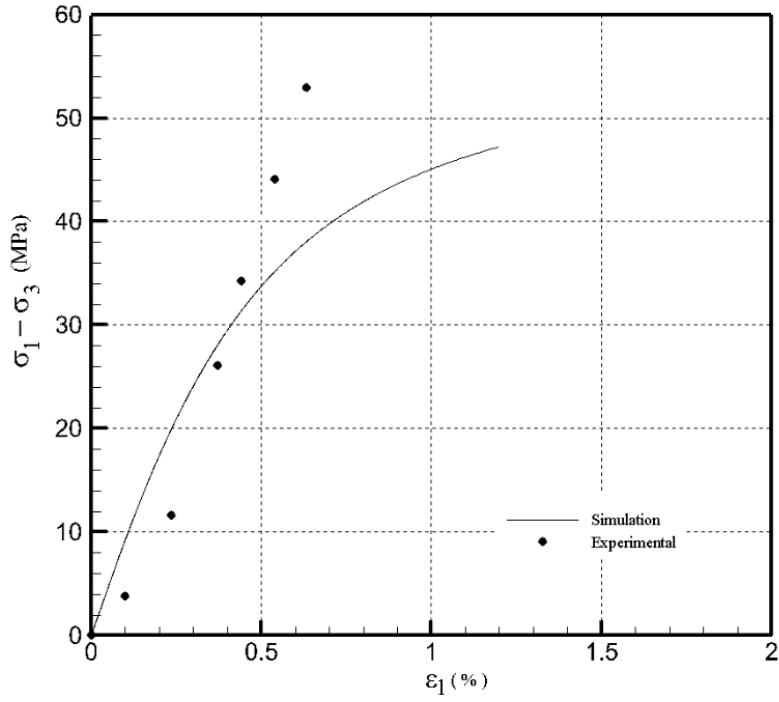
Finally, Figure 4. 14 and Figure 4.15 Show the comparisons between numerical predictions and experimental data for the bedding plane orientations equal to 0 and 90 degrees at the confining pressure of 40 *MPa*. Note that there was not experimental evidence for plotting volumetric strain at $\beta = 0$ degree. It is evident here that at higher confining pressures the model prediction is not in a good agreement with the experimental results. As mentioned earlier, the reason is that at higher pressures a non-linear form of the failure criterion is required.

Figure 4. 14 Numerical simulation of triaxial tests (deviatoric stress versus axial strain for horizontal bedding planes, $\beta = 0$, at P0 = 40 MPa)
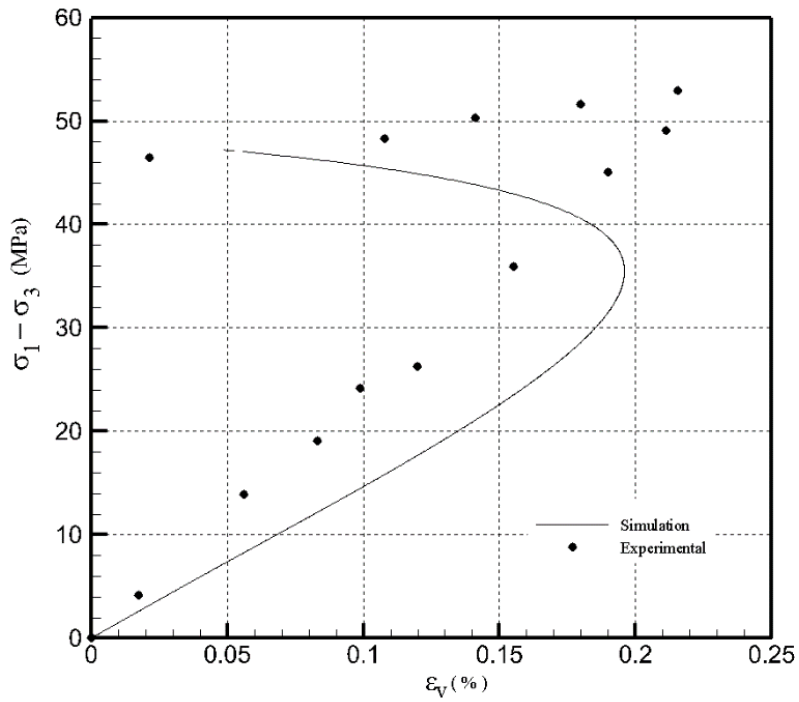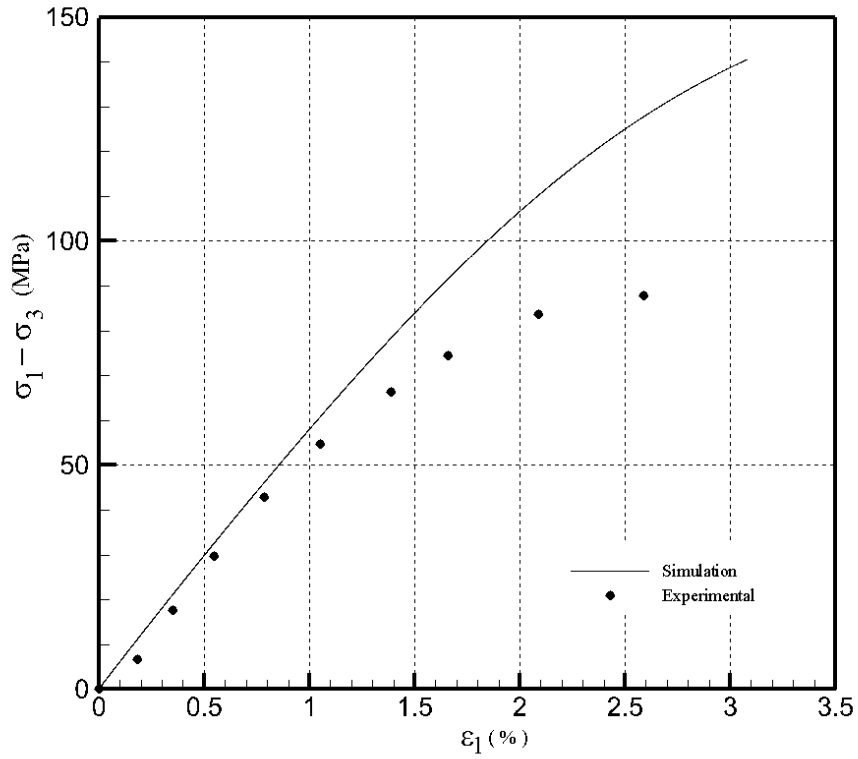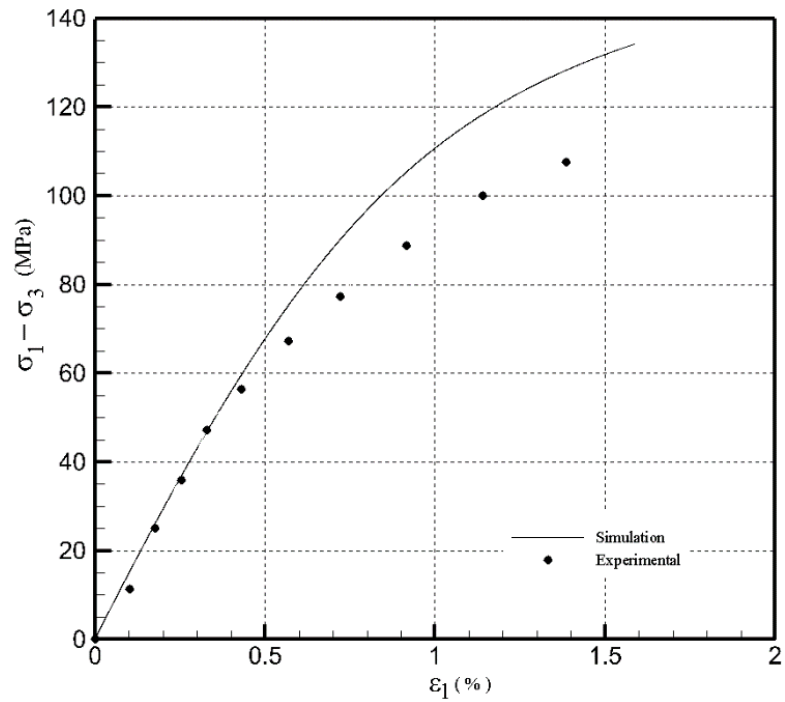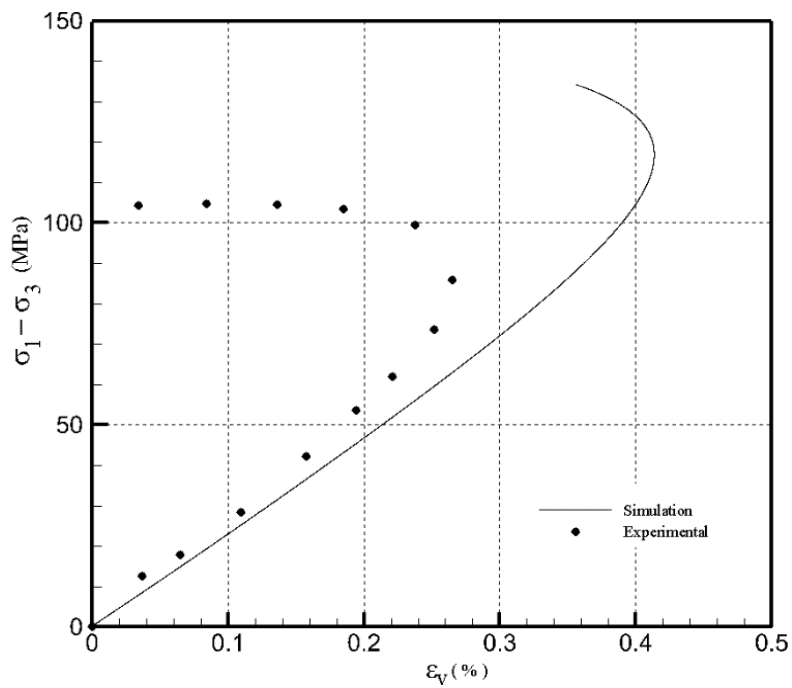
(a)

(b)

Figure 4.15   Numerical results of compression triaxial tests for vertical bedding planes, $\beta = 90°$, at $P_0 = 40$ MPa; (a) deviatoric stress versus axial strain and (b) volumetric strain, $\varepsilon_v = - (\varepsilon_x + \varepsilon_y + \varepsilon_z)$.

5. Finite element modelling of tunnel excavation in Tournemire shale

5.1 Introduction

Most of the practical engineering problems are non-linear and cannot be solved analytically. In view of this, different numerical techniques, such as Finite Element Method (FEM), are employed. In this approach, the domain is discretized into a number of finite elements and the numerical integration schemes are employed to solve the governing set of partial differential equations. As stated by Wood and Clayton, (1993), there are several sources of error that cause us to consider the FEM modelling predictions with caution. Those include modelling of the geometry of the problem, construction sequence, constitutive modelling and parameter selection, the general solution technique, etc.

As mentioned before, the shale studied in this research is an anisotropic rock, taken from the Tournemire site in the Massif Central region of France. It is known to be an appropriate host for chemical and nuclear waste storage and oil borehole formations. Therefore, an understanding of the deformation and failure mechanisms in this type of rock is of a significant importance. The problem addressed here deals with an assessment of damage around a tunnel excavated in Tournemire shale formation. The geometry, as well as the boundary and initial conditions related to this model, are taken from a study by Le and Nguyen, (2014). The constitutive relation incorporated in the FE analysis is based on a microstructure tensor approach that was discussed in chapter 2.

This chapter gives a brief description of the 3D FEM model of the tunnel excavation as well as a detailed presentation of the results of numerical analysis. The latter include the assessment of the deformation field around the tunnel for different orientations of the bedding planes. The analysis was carried out using the commercial code Abaqus/Standard in which the constitutive relation was incorporated.

5.2 FEM modelling of the tunnel excavation

Any commercial FE program is typically divided into separate modules for creating the geometry of the model, specification of material properties, assigning boundary, initial and loading conditions, and generating a mesh (discretization). After submitting the input file to the solver, the user can monitor the progress of the analysis and generate an output database. It should be noted that some finite element programs have interfaces that allow the users to implement their own constitutive equations when the existing material models included in the program material library are not adequate. For example user subroutine **UMAT** in Abaqus/Standard and user subroutine **VUMAT** in Abaqus/Explicit allow user-defined constitutive models to be added to the program, while the user subroutine **UEL** in Abaqus/Standard allows the creation of user-defined elements. The **UMAT** subroutine header is shown below:

```
SUBROUTINE UMAT ( STRESS, STATEV, DDSDDE, SSE, SPD, SCD,
                  RPL, DDSDDT, DRPLDE, DRPLDT, STRAN,
                  DSTRAN, TIME, DTIME, TEMP, DTEMP,
                  PREDEF, DPRED, CMNAME, NDI, NSHR,
                  NTENS, NSTATV, PROPS, NPROPS, COORDS,
                  DROT, PNEWDT, CELENT, DFGRD0, DFGRD1,
                  NOEL, NPT, LAYER, KSPT, KSTEP, KINC)
```

The key variables employed here are defined below.

DDSDDE: Jacobian (tangential) matrix of the constitutive model, $\partial \Delta \sigma / \partial \Delta \varepsilon,$ where $\Delta \sigma$ represents the stress increments and $\Delta \varepsilon$ is the strain increment. It should be pointed out that an unsymmetric equation solution for the user-defined material has to be invoked, otherwise the program will only use the symmetric part of **DDSDDE** which is one half the sum of the matrix and its transpose.

STRESS: This array is passed in as the stress tensor at the beginning of the increment and must be updated in this routine to represent the stress tensor at the end of the increment. If initial stresses are defined, this array will contain the initial stresses at the start of the analysis.

STATEV: An array containing the solution-dependent state variables. These are passed in as the values at the beginning of the increment, unless they are updated in other user subroutines in which case the updated values are passed in. In all cases **STATEV** must be returned as the values at the end of the increment.

SSE, SPD, SCD: Specific elastic strain energy, plastic dissipation, and creep dissipation, respectively. These are passed in as the values at the start of the increment and should be updated to the corresponding specific energy values at the end of the increment. They have no effect on the solution, except that they are used for energy output.

STRAN: An array containing the total strains at the beginning of the increment.

DSTRAN: An array of strain increments.

NSTATV: The number of solution-dependent state variables that are associated with this material type.

PROPS: A user-specified array of material constants associated with the user material.

In the following parts, the basic   steps that are employed in the analysis of the tunnel excavation problems are described.

5.2.1   *Modelling of the geometry*

This first step is to idealize the geometry of the problem. In this research both 2D and 3D finite element analyses are performed and the results are compared. The computational domain includes a cubic/square in which a tunnel has been excavated and the corresponding

initial stress is applied within the entire region. The in-plane size of the considered domain is $20\ m \times 20\ m$. For the 3D model, the depth along the tunnel axis is $18\ m$. The tunnel's length and diameter are $13\ m$ and $1.036\ m$, respectively. Plane strain conditions are imposed in 2D analysis.

5.2.2   *Assigning the material properties*

In the property module, material characteristics have to be specified. Space must be allocated to store each of the solution-dependent state variables defined in a user subroutine. In this study, the material properties of Tournemire shale, as identified in Chapter 3, have been employed.

5.2.3   *Applying loading, boundary and initial conditions*

For the tunnel excavation problem examined here, the initial, boundary and loading conditions are consistent with those employed in the study by Le & Nguyen, (2014). Figure 5.1 shows a cross-sectional view of the geometry of the problem. The analysis has been conducted for two different orientations of the bedding planes, viz. 45^0 and 90^0. The displacements along all external boundaries have been constrained (zero displacement) and the initial horizontal, vertical and axial stresses were taken as

$$\sigma_x = 4.4\ MPa\ \ ;\ \ \sigma_y = 6.5\ MPa\ \ ;\ \ \sigma_z = 2.2\ MPa$$

The excavation process is mathematically modelled by reducing traction on the tunnel wall boundary according to the tunnel drilling progress. The traction vectors that are initially assessed based on the in-situ stress field are reduced to zero at the end of the excavation.
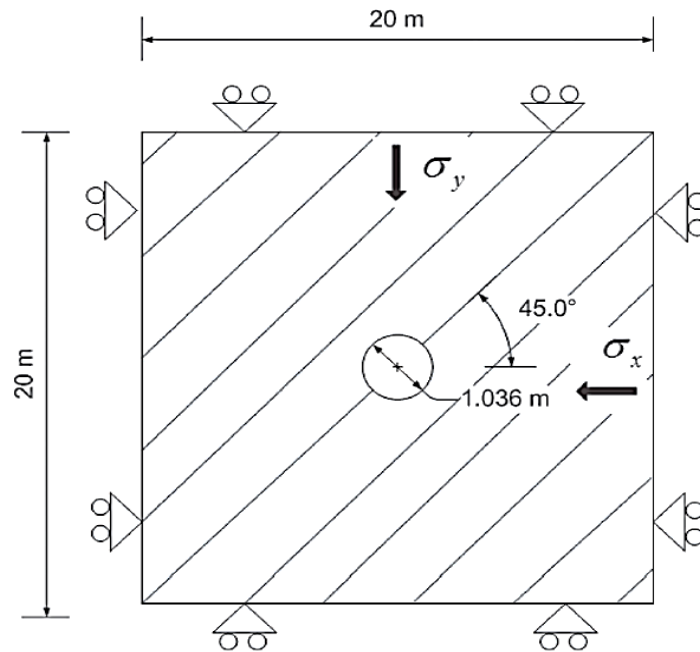
Figure 5. 1 The cross-sectional view of the model geometry and boundary conditions (after Le& Nguyen, 2014)

5.2.4   Mesh discretization and element type

In this study, the considered domain is discretized using 3D wedge elements with 6 nodes and linear interpolation for displacements. The total number of elements   is 43870 and the total number of degrees of freedom is 72036.

The 2D model has 2522 triangular plane strain elements with 3 nodes and a linear interpolation for displacement field. The total number of degrees of freedom is 5236. The computational domain and the corresponding discretization, for both 3D and 2D representation, are shown in figure 5. 2.

<div align="center">(a)   (b)</div>

<div align="center">Figure 5. 2   Computational domain and FE discretization in (a) 3D analysis (b) 2D analysis</div>
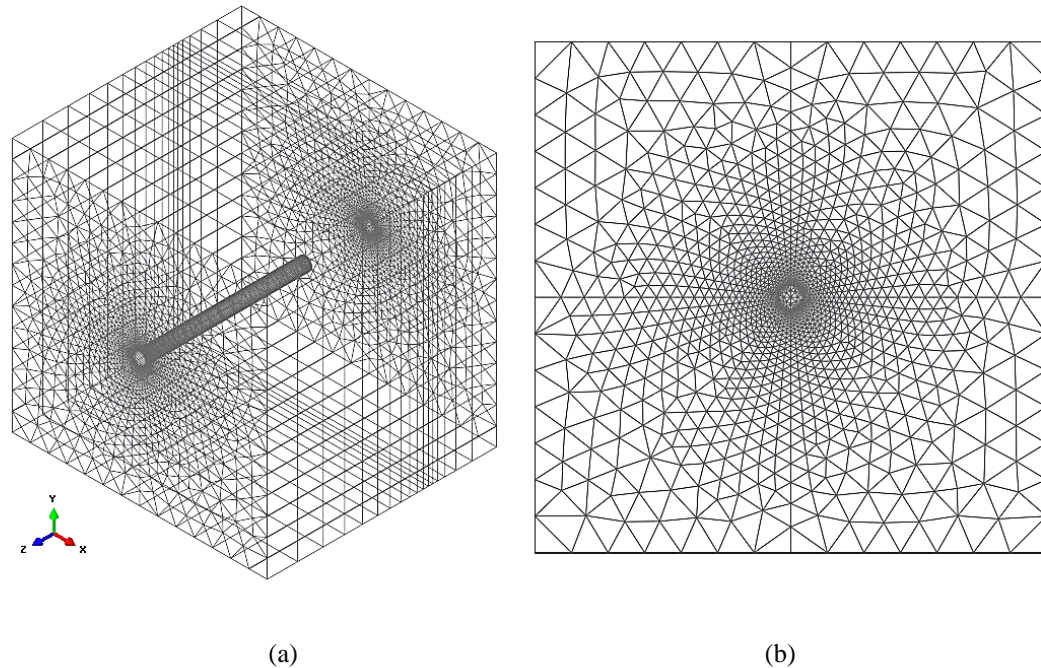
5.3   Numerical results and discussion

In this part the evolution of the mechanical response of the sedimentary rock surrounding the tunnel is simulated. The numerical results related to distribution of horizontal and vertical displacements (U_x, U_y), the damage/failure ratio (ϑ/η_f), and deviatoric plastic strain (ε_q^p) are presented.

First, the results of 3D analysis are discussed. Figure 5. 3 shows the horizontal and vertical displacement after excavation for the case of inclined bedding planes (45º). The displacement contours are superimposed on the deformed shape of the tunnel with a scale factor of 130. As can be seen, an approximately symmetric positive/negative horizontal displacement distribution is generated along the direction of bedding planes. For the vertical displacement contours, there is a similar symmetry in the distribution, while the

magnitudes are larger than those of horizontal displacements. Figure 5. 4 depicts the magnitude of displacements at the face of the tunnel as well as in a 3D view.

(a)   *(b)*

Figure 5. 3   (a) Horizontal displacements (b) Vertical displacements at the face of the tunnel for 3D analysis, β = 45°

(a)   *(b)*

Figure 5. 4   Displacement magnitudes (a) at face of the tunnel (b) along the length of tunnel, for 3D analysis, β = 45°

Figure 5. 5 represents the horizontal and vertical displacements in the neighbourhood of the tunnel face as obtained from two dimensional analysis ($\beta = 45°$). The distribution of

displacement contours is approximately the same as for 3D analysis; however, the predicted values are slightly lower.
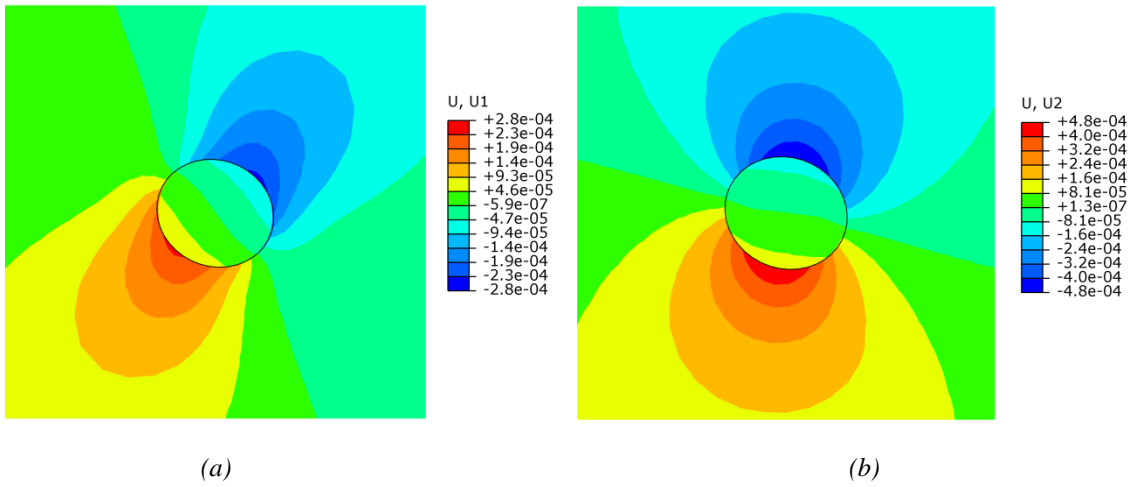

(a)   *(b)*
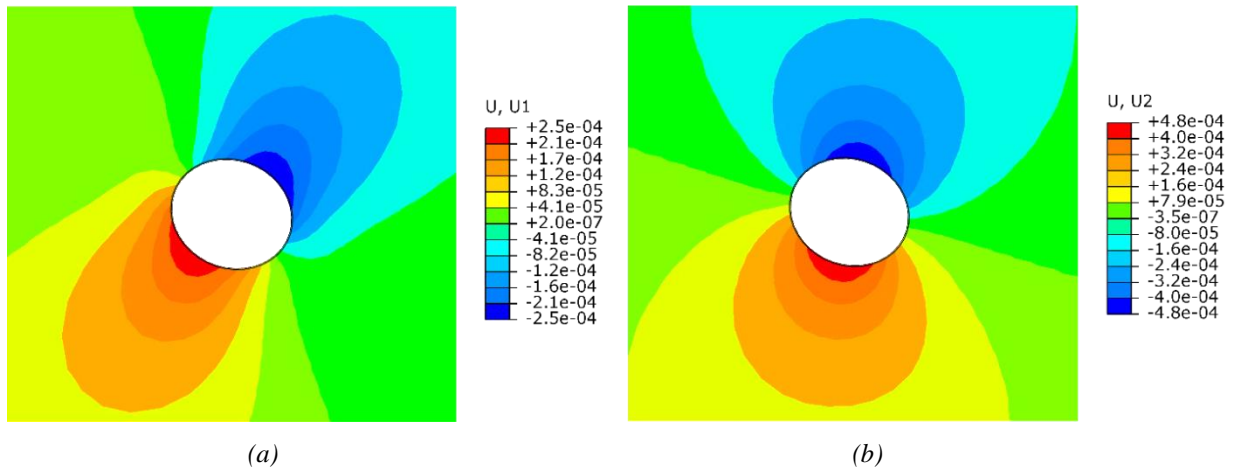
Figure 5. 5   (a) Horizontal displacements (b) Vertical displacements at the face of the tunnel for 2D analysis, β = 45º

Figure 5. 6 gives horizontal and vertical displacements after excavation obtained from 3D analysis for   the case when the bedding planes are horizontal (0º). The distribution of displacements also shows a symmetry with respect to the direction of the bedding planes. The deformed shape is now significantly different. As can be seen, the right side of the tunnel has negative horizontal displacements while the left side has positive displacements, i.e. in the direction of the x axis. The magnitudes are generally lower than those for the previous case of inclined bedding planes. At the same time, for the vertical component, the predicted values of displacements are larger than those obtained in the case of inclined bedding planes (45º).

Again, the absolute magnitudes of displacement vectors at the face of the tunnel as well as in a 3D view are depicted in Fig. 5.7.

(a)   *(b)*

Figure 5. 6   Horizontal displacements (b) Vertical displacements at the face of the tunnel for 3D analysis,

β = 0º

(a)   *(b)*
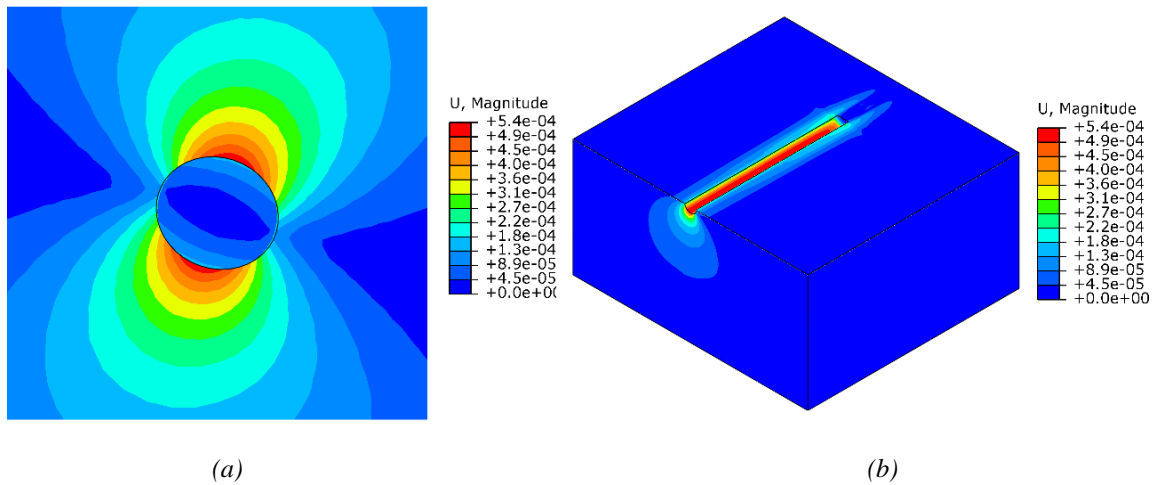
Figure 5. 7   Displacement magnitudes (a) at face of the tunnel (b) along the length of tunnel, for 3D
analysis, β = 0º

Figure 5. 8 presents the results of two dimensional analysis. Once more, the values and the
distribution of vertical and horizontal displacement are very similar to those obtained in 3D
analysis, indicating that the 2D approximation is fairly accurate here.

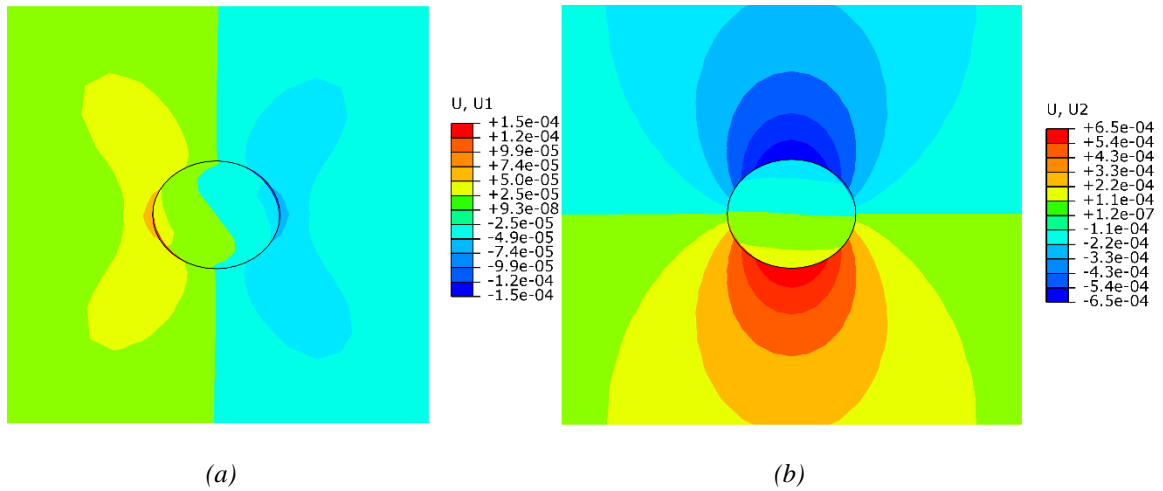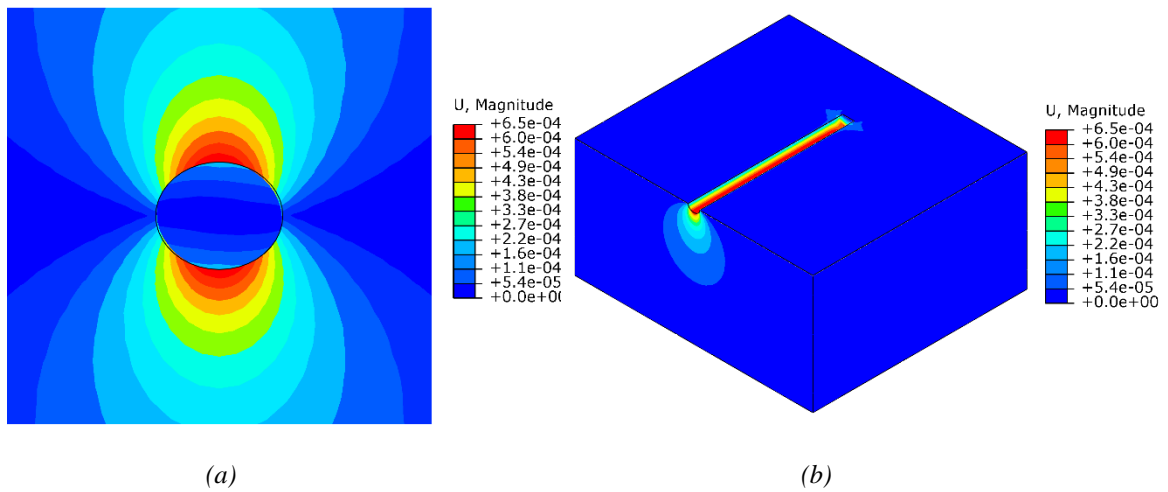*(a)*   *(b)*
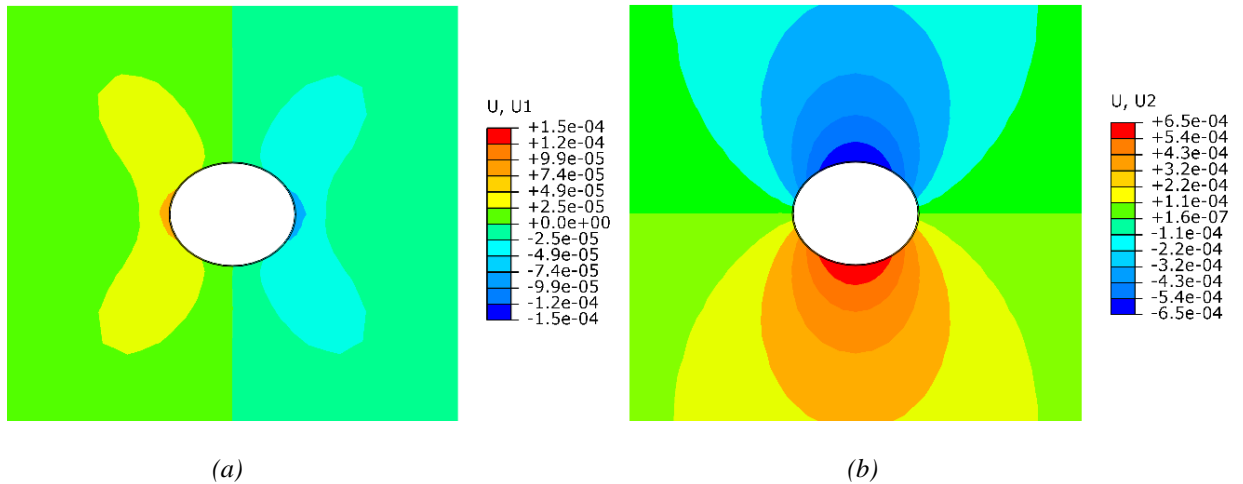
Figure 5. 8   (a) Horizontal displacement (b) Vertical displacement at the face of the tunnel for 2D analysis,
$\beta = 90º$

Figure 5. 9 (a) shows the distribution of the damage ratio (ϑ / η_f) obtained from 3D analysis

for the case of bedding planes at orientation of 45º. The parameters ϑ and η_f are defined

according to equations (2.50) and (2.48). Note that the ratio of ϑ / η_f varies between zero

and one $(0 \leq \vartheta / \eta_f \leq 1)$. Furthermore, $\vartheta / \eta_f = 1$, implies the onset of damage formation.

Here, the value of the damage ratio does not exceed 0.525, indicating that no cracks will

form immediately after the excavation. The maximum intensity of the damage ratio is along

the horizontal axis of the tunnel. Figure 5. 9 (b) shows the damage ratio distribution

obtained from 2D analysis. The maximum value of the damage ratio is now lower (0.503)

and the distribution of the damage domain is slightly different.

(a)   *(b)*

Figure 5. 1   Failure ratio ϑ / η_f at the face of the tunnel (a) 3D analysis (b) 2D analysis, β = 45°

Figure 5. 10 shows the evolution of the damage ratio (ϑ / η_f) for the case of horizontal bedding planes. The nature of the distribution is now different and the values are lower than those predicted for inclined bedding planes . For 3D analysis, the maximum value of 0.508 occurs now within a small region   at the end of the tunnel.   For a 2D analysis, the distribution is qualitatively similar to that corresponding to 3D case; however, the values of the damage ratio are slightly lower.
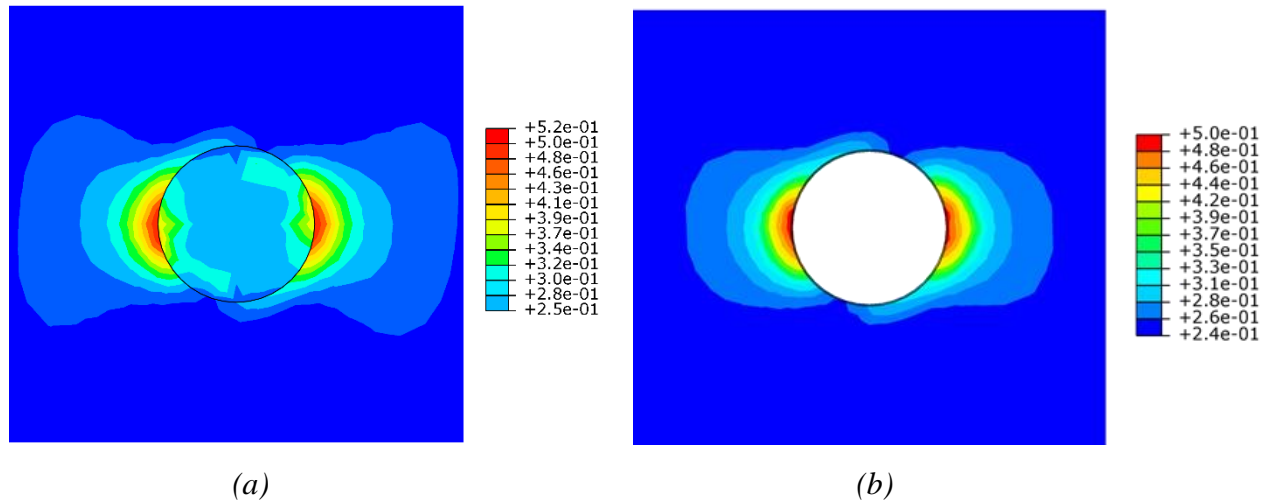
(a)   *(b)*
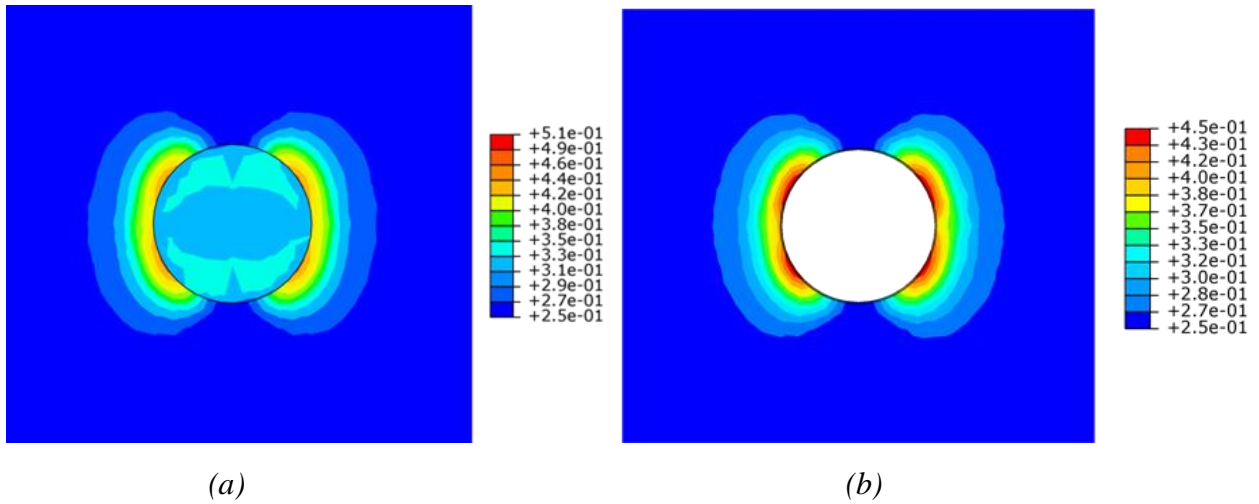
Figure 5. 2   Failure ratio ϑ / η_f at the face of the tunnel (a) 3D analysis (b) 2D analysis, $\beta = 0°$

Figure 5. 11 shows the distribution of the deviatoric plastic strain around the face of the tunnel for the case of inclined bedding planes. For 3D analysis, the calculated maximum value is 0.0009298 and it's attained along the horizontal axis. Again, for 2D analysis, the distribution is only marginally the same while the maximum value remains lower.

(a)   *(b)*
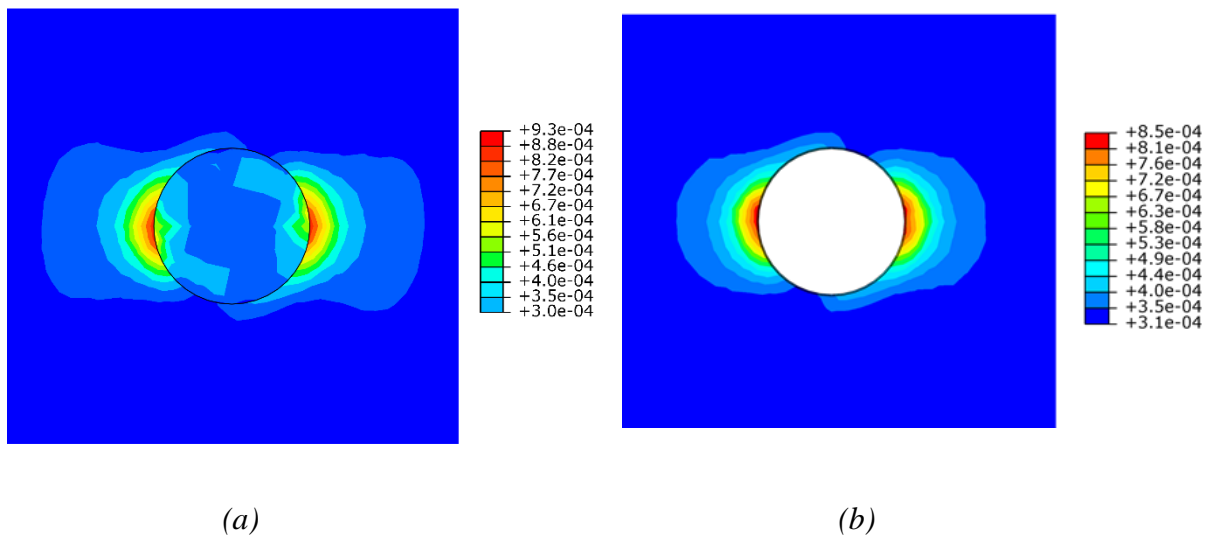
Figure 5. 3   Deviatoric plastic strain at the face of the tunnel (a) 3D analysis (b) 2D analysis, $\beta = 45°$

Finally, Figure 5. 12 shows the contours of deviatoric plastic strain for the case of horizontal bedding planes. The results are, generally, in agreement with those showing the distribution of damage ratio. Comparing the solution with that for inclined bedding planes, it is seen that the model predicts lower values of plastic distortion. This is consistent with the fact that the maximum strength is associated with configurations in which the bedding planes are either parallel or perpendicular to the loading direction. Once more, the results of 2D analysis, Figure 5.12b, display the same trend as those of 3D simulations, while the value of maximum plastic distortion is slightly lower in the entire domain.
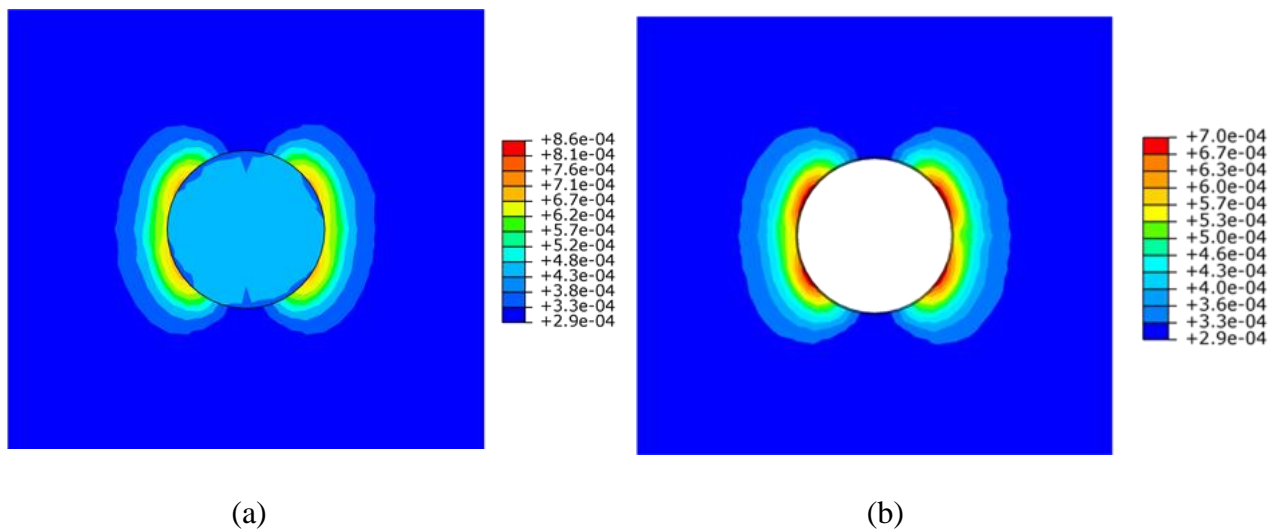

(a)   (b)

Figure 5. 4   Deviatoric plastic strain at the face of the tunnel (a) 3D analysis (b) 2D analysis,
β = 0º

6.   Concluding remarks

Many geomaterials display a structural anisotropy which is closely related to their microstructure. In this study the main focus was on a specific sedimentary rock known as Tournemire shale. This shale was formed by compaction, cementation or crystallization of successive layers of deposited material. It is characterized by the presence of closely spaced bedding planes and exhibits a strong directional dependence of strength as well as deformation properties. Its mechanical behaviour is transversely isotropic and the plane of isotropy is the bedding plane. An understanding of the mechanical behaviour of Tournemire shale is of a significant importance due to its widespread applications in many types of geotechnical projects, including oil industry and nuclear waste storage.

Extensive triaxial compression tests under different confining pressures have been conducted on this rocks. The results generally show that the failure mode depends on confining pressure and loading orientation relative to the bedding planes. The volumetric strain is mainly compressive and the transition to dilatancy occurs only in the zone near the peak stress. Moreover, the maximum failure strength is associated with configurations in which the bedding planes are either parallel or perpendicular to the loading direction and the minimum strength is typically associated with failure along the weakest plane, which corresponds to sample orientations within the range $30^{\circ} - 60^{\circ}$.

The experimental results offer a comprehensive database to establish and validate constitutive models for anisotropic rocks. In this work, the mathematical formulation incorporating a microstructure tensor approach (Pietruszczak & Mroz, 2001) has been chosen for the description of orientation dependent characteristics of Tournemire shale. A plasticity framework incorporating an anisotropic deviatoric hardening model has also been presented. The condition at failure have been described by employing the Mohr-Coulomb failure criterion.

The elastoplastic constitutive relation for modeling the mechanical behaviour of Tournemire shale, represents a differential equation that cannot be reduced to a finite relation between stress and strain tensors due to nonlinear/history dependent response. Therefore an explicit integration scheme has been developed and employed for obtaining the numerical solution.

Using the experimental results reported by Niandou et al. (1997), the material parameters/function, including strength descriptors associated with the failure criterion, coefficients of best-fit approximation governing their distribution, and the hardening parameters, have been identified. Using those parameters, the numerical simulations of a number of triaxial tests were conducted and the results compared with the experimental data in order to verify the performance of the model.

After the verification stage, the formulation was incorporated in a commercial FE code (Abaqus/standard) using the **UMAT** interface and was then applied to a numerical analysis of a tunnel excavation within the anisotropic rock mass. The numerical results of 2D and 3D simulations for two different orientations of the bedding planes, 45 and 0º, have been compared. Those included the distribution of the damage ratio$\left(\dfrac{\eta}{\eta_{f_0}} \right)$, vertical and horizontal displacements and the deviatoric plastic strains. It was demonstrated that the 2D approximation gives quite a reasonable approximation for the problem considered in this work.

In general, the methodology presented is simple enough to be used for the solution of practical engineering problems. Some concluding remarks associated with this study are as follows

- Availability of the experimental data for specification of material constants as well as the verification of predictive abilities of the model are two important concerns for choosing an appropriate approach.

- Triaxial test results on inclined samples are not very reliable because the triaxial apparatus imposes kinematic constraints and the deformation field is not uniform.

- For the safety analysis of structures constructed in geological formations with the directional dependence of strength, it is important to develop constitutive models able to account for influence of structural anisotropy.

- The main concern with most of the anisotropic formulations is the fact that they employ numerous material parameters and/or functions. Identifying these parameters requires an extensive experimental program which needs to be conducted in relation to material.

- In this work the anisotropic formulation was based solely on one scalar anisotropy parameter which is a homogeneous function of stress of degree zero. Thus, the value of this parameter does not depend on the value of stress but only on the relative orientation of the principal stress triad with respect to the eigenvectors of the microstructure tensor.

- An associated flow rule used with the Mohr‑Coulomb yield criterion would over-predicts the plastic volumetric deformation (dilatancy) compared to experimental results (Paterson & Wong, 2005). Therefore, a non-associated flow rule was implemented.

- For an anisotropic material, the compressive strength is sensitive to the value of the intermediate principal stress, since it affects the evolution of the anisotropy parameter. However for an isotropic material, $\eta_f = \eta_{f_0} = \text{const.}, (A_{ij} = 0),$ the results based on the Mohr Coulomb criterion are independent of the intermediate principal stress.

- Comparison between numerical simulations and experimental results show that the model which is used in this research is capable of reproducing the main features in the mechanical response of the transversely isotropic Tournemire shale. For

instance, under higher confining pressure, the mechanical strength increases and inelastic deformations turn out to be more noticeable. The transition from volumetric compaction to dilatancy is also accounted for.

- At higher confining pressures the model prediction is not in a good agreement with the experimental results. Thus, at higher pressures a non-linear form of the failure function is required to predict the mechanical behavior of Tournemire shale. The results associated with the quadratic failure function can be found in the study by Pietruszczak et al., (2002).

- Strain softening due to strain localization under lower confining pressures cannot be modeled here, since the formulation discussed is limited to the strain hardening range. Due to this reason the numerical simulations were stopped at the point where $\dfrac{\eta}{\eta_f} \leq 0.98$. The strain softening needs to be considered as a boundary-value problem.

- In analysing the initial boundary-value problems using finite element methodologies, the basic unknowns are the displacement rates. The local strain rates that are determined from the kinematic relations can be used in the constitutive law for evaluating the stress rates. The integration algorithms should be written in a strain-controlled regime.

- For the tunnel excavation problem analysed in this thesis, 2D analysis predicts nearly the same values of displacements as 3D analysis. On the other hand, 3D analysis predicts slightly higher values of plastic strain and damage ratio than 2D analysis.

- The damage ratio and plastic strain obtained from both 2D and 3D analyses is larger when the bedding plane orientation is 45° compared to a horizontal bedding plane. This is consistent with the fact that maximum compressive strength is either at $\beta = 0°$ or $\beta = 90°$ and the minimum value is usually within the range $30° \leq \beta \leq 60°$.

Finally, it should be noted that the time dependency of the mechanical behaviour of Tournemire shale is quite important, particularly in relation to the deep excavation problems. Therefore, for long term stability study of structures, it will be necessary to develop time dependent constitutive models. Moreover, given the existing experimental data, the compressive strength properties of Tournemire shale are not linear in terms of pressure. Choosing a higher order terms in the failure criterion will lead to more reliable results.

References

Abelev, A. V., & Lade, P. V. (2004). Characterization of Failure in Cross-Anisotropic Soils. Journal of Engineering Mechanics, 130(5), 599–606.

Ajalloeian, R., & Lashkaripour, G. R. (2000). Strength anisotropies in mudrocks. Bulletin of Engineering Geology and the Environment, 59(3), 195–199.

Al-Harthi, A. A. (1998). Effect of planar structures on the anisotropy of Ranyah sandstone, Saudi Arabia. Engineering Geology, 50(1-2), 49–57.

Amadei, B. (1983). Rock Anisotropy and the Theory of Stress Measurements (Vol. 2). Springer Science & Business Media.

Angabini, A. (2003). Anisotropy of rock elasticity behavior and of gas migration in a Variscan Carboniferous rock mass in the South Limburg, The Netherlands. Engineering Geology, 67(3-4), 353–372.

Arora, V. (1987). Strength and deformational behaviour of jointed rocks. (Doctoral dissertation, Indian Institute of Technology, Delhi).

Arthur, J. R. F., & Menzies, B. K. (1972). Inherent anisotropy in a sand. Géotechnique, 22(1), 115–128.

Attewell, P. B., & Sandford, M. R. (1974). Intrinsic shear strength of a brittle, anisotropic rock—I. International Journal of Rock Mechanics and Mining Sciences & Geomechanics Abstracts, 11(11), 423–430.

Behrestaghi, M. H. N., Seshagiri Rao, K., & Ramamurthy, T. (1996). Engineering geological and geotechnical responses of schistose rocks from dam project areas in India. Engineering Geology, 44(1-4), 183–201.

Boehler, J. (1978). Lois de comportement anisotrope des milieux continus. Journal de mécanique, 17(2), 153-190.

Boehler, J., & Sawczuk, A. (1970). Equilibre limite des sols anisotropes. J. Mécanique, 9, 5-33.

Brown, E., Richards, L., & Barr, M. (1977). Shear strength characteristics of Delabole slates. In Proceedings of the conference rock engineering, Newcastle upon Tyne (pp. 33-51).

Casagrande, A., & Carillo, N. (1944). Shear failure of anisotropic materials. Journal of Boston Society of Civil Engineers. Journal of the Boston Society of Civil Engineers, 31(4), 122-135.

Cazacu, O., & Cristescu, N. (1998). A new anisotropic failure criterion for transversely isotropic solids. Mechanics of Cohesive-frictional Materials, 3(1), 89-103.

Chappell, B. A. (1990). Moduli stress dependency in anisotropic rock masses. Mining Science and Technology, 10(2), 127–143.

Chen, L., Shao, J. F., & Huang, H. W. (2010). Coupled elastoplastic damage modeling of anisotropic rocks. Computers and Geotechnics, 37(1-2), 187–194.

Chen, L., Shao, J. F., Zhu, Q. Z., & Duveau, G. (2012). Induced anisotropic damage and plasticity in initially anisotropic sedimentary rocks. International Journal of Rock Mechanics and Mining Sciences, 51, 13–23.

Chenevert, M. E., & Gatlin, C. (2013). Mechanical Anisotropies of Laminated Sedimentary Rocks. Society of Petroleum Engineers Journal, 5(01), 67–77.

Colak, K., & Unlu, T. (2004). Effect of transverse anisotropy on the Hoek–Brown strength parameter "mi" for intact rocks. International Journal of Rock Mechanics and Mining Sciences, 41(6), 1045–1052.

Cowin, S. C. (1986). Fabric dependence of an anisotropic strength criterion. Mechanics of Materials, 5(3), 251–260.

Deklotz, E. J., Brown, J. W., & Stemler, O. A. (1966, January 1). Anisotropy of a Schistose Gneiss. In 1st ISRM Congress. International Society for Rock Mechanics.

Donath, F. (1964). Strength variation and deformational behavior in anisotropic rock. State of Stress in the Earth's Crust, 281-297.

Duveau, G., Shao, J. F., & Henry, J. P. (1998). Assessment of some failure criteria for strongly anisotropic geomaterials. Mechanics of Cohesive-Frictional Materials, 3(1), 1–26.

Hill, R. (1948). A Theory of the Yielding and Plastic Flow of Anisotropic Metals. Proceedings of the Royal Society A: Mathematical, Physical and Engineering Sciences, 193(1033), 281–297.

Hoek, E. (1964). Fracture of anisotropic rock. Journal of the South African Institute of Mining and Metallurgy, 64(10), 501-523.

Hoek, E. (1983). Strength of jointed rock masses. Géotechnique, 33(3), 187–223.

Hoek, E., & Brown, E. T. (n.d.). Emperical Strength Criterion for Rock Masses. Journal of Geotechnical and Geoenvironmental Engineering, 106(ASCE 15715).

Horino, F., & Ellickson, M. (1970). A method for estimating strength of rock containing planes of weakness (Vol. 7449). US Dept. of Interior, Bureau of Mines.

Jaeger, J. C. (2009). Shear Failure of Anistropic Rocks. Geological Magazine, 97(01), 65.

Karakul, H., Ulusay, R., & Isik, N. S. (2010). Empirical models and numerical analysis for assessing strength anisotropy based on block punch index and uniaxial compression tests. International Journal of Rock Mechanics and Mining Sciences, 47(4), 657–665.

Ken-Ichi, K. (1984). Distribution of directional data and fabric tensors. International Journal of Engineering Science, 22(2), 149–164.

Kirkgard, M. M., & Lade, P. V. (1993). Anisotropic three-dimensional behavior of a normally consolidated clay. Canadian Geotechnical Journal, 30(5), 848–858.

Kwasniewski, M. (1993). Mechanical behavior of anisotropic rocks. Comprehensive Rock Engineering, 1, 285-312.

LeA.D., & NguyenT.S. (2014). Hydromechanical response of a bedded argillaceous rock formation to excavation and water injection1. Canadian Geotechnical Journal, 52(1), 1-17.

Martin McCabe, W., & Koerner, R. M. (1975). High pressure shear strength investigation of an anisotropic mica schist rock. International Journal of Rock Mechanics and Mining Sciences & Geomechanics Abstracts, 12(8), 219–228.

McLamore, R., & Gray, K. E. (1967). The Mechanical Behavior of Anisotropic Sedimentary Rocks. Journal of Engineering for Industry, 89(1), 62.

Nasseri, M. H. ., Rao, K. ., & Ramamurthy, T. (2003). Anisotropic strength and deformational behavior of Himalayan schists. International Journal of Rock Mechanics and Mining Sciences, 40(1), 3–23.

Niandou, H. (1994). Etude du comportement rhéologique et modélisation de l'argilite de Tournemire. Applications à la stabilité d'ouvrages souterrains (Doctoral dissertation).

Niandou, H., Shao, J. F., Henry, J. P., & Fourmaintraux, D. (1997). Laboratory investigation of the mechanical behaviour of Tournemire shale. International Journal of Rock Mechanics and Mining Sciences, 34(1), 3–16.

ODA, M., KOISHIKAWA, I., & HIGUCHI, T. (1978). Experimental study of anisotropic shear strength of sand by plane strain test. Soil and Foundations, 18(1), 25–38.

Pariseau, W. G. (1968, January 1). Plasticity Theory For Anisotropic Rocks And Soil. American Rock Mechanics Association. In The 10th US Symposium on Rock Mechanics (USRMS). American Rock Mechanics Association.

Paterson, M. S., & Wong, T. (2005). Experimental Rock Deformation - The Brittle Field. Springer Science & Business Media.

Pietruszczak, S. (1999). On inelastic behaviour of anisotropic frictional materials. Mechanics of Cohesive-frictional Materials, 4(3), 281–293.

Pietruszczak, S. (2010). Fundamentals of plasticity in geomechanics. Crc Press.

Pietruszczak, S., Lydzba, D., & Shao, J. . (2002). Modelling of inherent anisotropy in sedimentary rocks. International Journal of Solids and Structures, 39(3), 637–648.

Pietruszczak, S., & Mroz, Z. (2000). Formulation of anisotropic failure criteria incorporating a microstructure tensor. Computers and Geotechnics, 26(2), 105–112.

Pietruszczak, S., & Mroz, Z. (2001). On failure criteria for anisotropic cohesive-frictional materials. International Journal for Numerical and Analytical Methods in Geomechanics, 25(5), 509–524.

Pomeroy, C. D., Hobbs, D. W., & Mahmoud, A. (1971, May). The effect of weakness-plane orientation on the fracture of Barnsley Hards by triaxial compression. In International Journal of Rock Mechanics and Mining Sciences & Geomechanics Abstracts (Vol. 8, No. 3, pp. 227-238). Pergamon.

Qiang, Y., Zhongkui, L., & Tham, L. G. (2001). An explicit expression of second-order fabric-tensor dependent elastic compliance tensor. Mechanics Research Communications, 28(3), 255–260.

Ramamurthy, T. (1993). Strength and modulus responses of anisotropic rocks. Comprehensive rock engineering, 1(13), 313-29.

Ramamurthy, T., Rao, Gv., & Singh, J. (1988). A Strength Criterion for Anisotropic Rocks.

Rao, K. S., Rao, G. V., & Ramamurthy, T. (1986). A strength criterion for anisotropic rocks. Ind Geotech J, 16(4), 317-333.

Salager, S., François, B., Nuth, M., & Laloui, L. (2012). Constitutive analysis of the mechanical anisotropy of Opalinus Clay. Acta Geotechnica, 8(2), 137–154.

Schmitt, L., Forsans, T., & Santarelli, F. J. (1994). Shale testing and capillary phenomena. International Journal of Rock Mechanics and Mining Sciences & Geomechanics Abstracts, 31(5), 411–427.

Tien, Y., & Tsao, P. (2000). Preparation and mechanical properties of artificial transversely isotropic rock. International Journal of Rock Mechanics and Mining Sciences, 37(6), 1001-1012.

Tsai, S. W., & Wu, E. M. (1971). A General Theory of Strength for Anisotropic Materials. Journal of Composite Materials, 5(1), 58–80.

Valès, F., Nguyen Minh, D., Gharbi, H., & Rejeb, A. (2004). Experimental study of the influence of the degree of saturation on physical and mechanical properties in Tournemire shale (France). Applied Clay Science, 26(1-4), 197–207.

Walsh, J. B., & Brace, W. F. (1964). A fracture criterion for brittle anisotropic rock. Journal of Geophysical Research, 69(16), 3449–3456.